Aerial and Space-borne Seismology on Venus: Viability and Design Implications for Future Missions

Quentin Brissaud [https://orcid.org/0000-0001-8189-4699][*1], Chenxi Kong [https://orcid.org/0009-0002-6758-105X][2], John Wilding [https://orcid.org/0000-0002-0914-2078][2], Anna J. P. Gülcher [https://orcid.org/0000-0001-5999-3463][3], Jennifer M. Jackson [https://orcid.org/0000-0002-8256-6336][2], Marouchka Froment [https://orcid.org/0000-0002-2980-8711][1], Sven Peter Näsholm [https://orcid.org/0000-0001-9107-4002][1,4], Raphaël F. Garcia [https://orcid.org/0000-0003-1460-6663][7], Celine Marie Solberg [https://orcid.org/0009-0001-4683-7792][4,5], and Iris van Zelst [https://orcid.org/0000-0003-4698-9910][6]

[1]NORSAR, Gunnar Randers vei 15, Kjeller, Norway
[2]Seismological Laboratory, California Institute of Technology
[3]Center for Space and Habitability, University of Bern, Bern, Switzerland
[4]Department of Informatics, University of Oslo, Gaustadalléen 23B, 0373 Oslo, Norway
[5]Kongsberg Defence & Aerospace, Drengsrudbekken 12, 1383 Asker, Norway
[6]School of GeoSciences, University of Edinburgh, Edinburgh, UK
[7]Institut Supérieur de l'Aéronautique et de l'Espace ISAE-SUPAERO, Université de Toulouse, Toulouse, France

Abstract.

Venus' evolution remains a mystery because of the lack of in-situ geophysical data to constrain its interior structure. Recently-selected planetary missions including VERITAS (NASA), DAVINCI+ (NASA), and EnVision (ESA) will investigate the planet's interior, surface, and atmospheric chemistry. However, none of these missions includes sensors capable of probing Venus' crustal and mantle properties with high accuracy. Ground deployments of seismometers are challenging on Venus due to its high surface temperature and pressure. Instead, balloon pressure measurements and airglow observations – monitoring of the continuous glow of the Venus' upper atmosphere caused by chemical and radiative processes – have been suggested as compelling alternatives to surface deployments. However, it is critical to accurately assess the potential of such missions under realistic conditions of geology, atmospheric states, network geometry, and seismicity scenarios using physics-based modeling. Here, we employ a probabilistic framework to investigate detection probabilities as a function of Signal-to-Noise Ratio (SNR) for airglow and balloon missions using numerical wave simulations, thermodynamically-consistent seismic velocity models, and realistic seismicity models. Our results demonstrate that the probability of detecting a single venusquake event at SNR > 1 over a 6-month mission is around 65% across an entire 3-balloons network of about 5000 km extent. We obtain over 90% probability when the venusquake monitoring is based on either nightglow or dayglow imager data. Seismo-volcanic sequences could significantly enhance detectability if high seismic activity occurs at multiple volcanoes. Longer duration missions that include both airglow and balloon-borne sensors could therefore allow seismic wave measurements over a broader range of frequencies.

Plain Language Summary. The interior of Venus remains a mystery because we lack seismic data. Such data were key to constrain the Moon's and Mars' subsurface. While upcoming missions will study Venus' surface and atmosphere, they will not carry instruments capable of detecting seismic waves from the ground. Because Venus' surface is extremely hot and under intense pressure, deploying traditional seismometers is challenging. As an alternative, scientists have proposed using high-altitude balloons and orbiting airglow cameras to detect pressure waves or light emissions in the atmosphere that may be triggered by venusquakes. In this study, we apply physics-based models and probabilistic methods to evaluate how well balloon and airglow observations would detect seismic events under realistic atmospheric and geological conditions. We show that a balloon network covering about 5,000 km could detect at least one venusquake with up to 65% chance over a 6-month mission. The detection rates are even higher—above 90%—when using airglow observations from orbit. These findings suggest that future missions combining these techniques will provide valuable seismic data to reveal Venus' internal structure.

*Corresponding author: Quentin Brissaud (quentin@norsar.no)

Key Points

- We built a probabilistic framework to assess the detectability of venusquakes from its atmosphere and space using physics-based simulations
- We obtain high detectability levels for 6 months-long missions combining balloons and airglow giving a high-resolution view of the interior
- Prior seismic velocity models, noise levels, and wave periods are the most critical aspects driving detectability

1 Introduction

The evolution and present dynamics of Venus remain a mystery due to the lack of in-situ geophysical data to constrain its atmosphere and interior structure. To address important scientific questions regarding Venus' past and present conditions and its habitability, NASA and ESA have selected three planetary missions that will investigate aspects of its deep interior, its surface, and atmospheric chemistry (*Widemann et al.*, 2023). However, the collection of seismic data, such as performed on Mars by the InSight seismometer (*Lognonné et al.*, 2023), is key to developing accurate and precise models of the planet's interior. Unfortunately, the high pressure and temperature conditions at the surface of Venus will most likely prevent any long-duration deployments of seismic instruments beyond a few months (*Kremic et al.*, 2020). Recently, the seismo-acoustic community has proposed new methodologies, called balloon-based and airglow-based seismology, to alleviate the need for ground-based measurements (*Krishnamoorthy et al.*, 2019). As seismic waves couple to the atmosphere, they excite low-frequency acoustic waves – infrasound – in the atmosphere which propagate to high altitudes. These acoustic waves carry information about the source and the subsurface, allowing subsurface seismic imaging to be performed from high altitudes. Several detections of seismic waves in pressure waveforms recorded by stratospheric balloon platforms have already been reported in recent years on Earth (*Brissaud et al.*, 2021; *Garcia et al.*, 2022). Balloons equipped with microbarometers flying in Venus' cloud layer between 45 to 60 km altitude, where atmospheric pressure and temperatures are similar to Earth's surface, could therefore detect the small pressure fluctuations induced by Venusquake ground motion. At higher altitudes, above 90 km, acoustic waves can affect the transport of O_2 atoms in the nightglow and their adiabatic temperature signature can perturb CO_2 atoms in the dayglow. Light emissions produced by such perturbations can be sensed by satellites equipped with airglow cameras (*Garcia et al.*, 2024).

Assessing the feasibility of balloon-borne seismology in the Venus context is critical in future mission concept design. In particular, it remains unclear what would be the required mission duration to ensure the detection of significant seismic quakes. Interestingly, owing to Venus' high-density atmosphere, the coupling between the ground and the atmosphere is significantly stronger than on Earth, which could enable the detection of lower-magnitude venusquakes (*Averbuch et al.*, 2023). Yet, the absence of global plate tectonics on Venus likely drastically reduces the occurrence of large-magnitude quakes (e.g., *Van Zelst et al.*, 2024a). Recently, *Garcia et al.* (2024), referred to in the rest of the paper as *Garcia et al.* (2024), provided a preliminary framework to address these research questions for mission scenarios using either a ground-based seismic instrument, a single atmospheric balloon equipped with a microbarometer, or an airglow imager. *Garcia et al.* (2024) determined the minimum number of events needed to obtain an arbitrary 66% detection probability for a seismic event from each of these instruments. *Garcia et al.* (2024) concluded that about 100 M_w5 events over a 6-month balloon mission, or less than 10 events for an airglow mission should be enough to ensure the detection of one seismic event with a 66% probability.

There are several limiting assumptions in *Garcia et al.* (2024) that deserve further investigation: (1) The seismic activity was considered to be homogeneous over the whole planet (as in *Van Zelst et al.*, 2024a), despite the non-uniform spatial distribution of regions with more seismically-active potential, such as Venusian rifts, or dozens of "corona" structures with a non-random global distribution proposed to be geologically active (*Davaille et al.*, 2017; *Gülcher et al.*, 2020; *Cascioli et al.*, 2025) – circular volcano-tectonics features defined by a (partial) ring of closely-spaced fractures; (2) Seismic amplitudes were modeled using an empirical relationship relating magnitude to peak seismic velocity, which was designed for Earth scenarios. Thus, investigating the effect of seismic properties on detectability was not possible; (3) Only single-instrument and single-balloon detectability was estimated. Yet, to retrieve subsurface properties at various scales, multi-instrument combined airglow-balloon measurements of the same events should be performed, as acoustic-to-airglow coupling is less efficient at high frequencies (*Kenda*, 2018). This means that determining the probability of observing the same event across all instruments is critical for future missions; (4) Results were provided at 66% confidence level. Yet, mission designs should likely consider higher confidence levels to ensure the detection of seismic events; (5) The study used a binary condition to define detectability, which is that signal amplitudes exceed the noise level, but details such as the Signal-to-Noise Ratio (SNR), i.e., ratio of amplitude over noise level, of detectable events were not considered. While this was a reasonable first step, the ability to detect signals at sufficiently high SNR is critical for successful subsurface velocity inversions; (6) Finally, only seismic events of seismo-tectonic origin were considered, and seismo-volcanic events were not specifically included in the analysis. Yet, recent volcanic activity on Venus has been detected in Magellan data (*Herrick and Hensley*, 2023; *Sulcanese et al.*, 2024) and could constitute a major source of seismic waves.

In this contribution, we build a more comprehensive physics-based probabilistic framework to address these limitations and produce robust detectability estimates of seismic waves on Venus. While Venus' seismicity remains mostly unknown, here we consider and adapt two recently proposed seismicity models (*Sabbeth et al.*, 2023; *Van Zelst et al.*, 2024a) to account for the spatial heterogeneities in seismicity (Section 2.1). Instead of relying on empirical amplitude equations, we model the seismic wave propagation and coupling numerically, for realistic seismic and atmospheric media (Section 2.2). Additionally, we produce detectability estimates for multi-instrument missions deploying balloon networks, or combining a balloon and an airglow imager (Section 2.3). Importantly, our probabilistic framework produces detection probabilities in terms of SNR, which facilitates sensitivity analysis at any noise level (Section 3). Finally, we investigate the detectability of Earth seismo-volcanic sequences, serving as a proxy for volcanism on Venus (Section 4).

2 Methods

Our objective is to estimate the detection probability of seismic waves in balloon pressure signals exceeding a given SNR along given balloon trajectories. This is based on a four-step procedure: (1) we compute the probability of venusquakes, over a given magnitude, occurring at each surface location based on magnitude-frequency distribution models, (2) we determine the pressure amplitude at each distance of venusquake-induced infrasound at the balloon altitude using numerical simulations, (3) we estimate the likelihood of observing a signal above a given SNR from a fixed balloon location

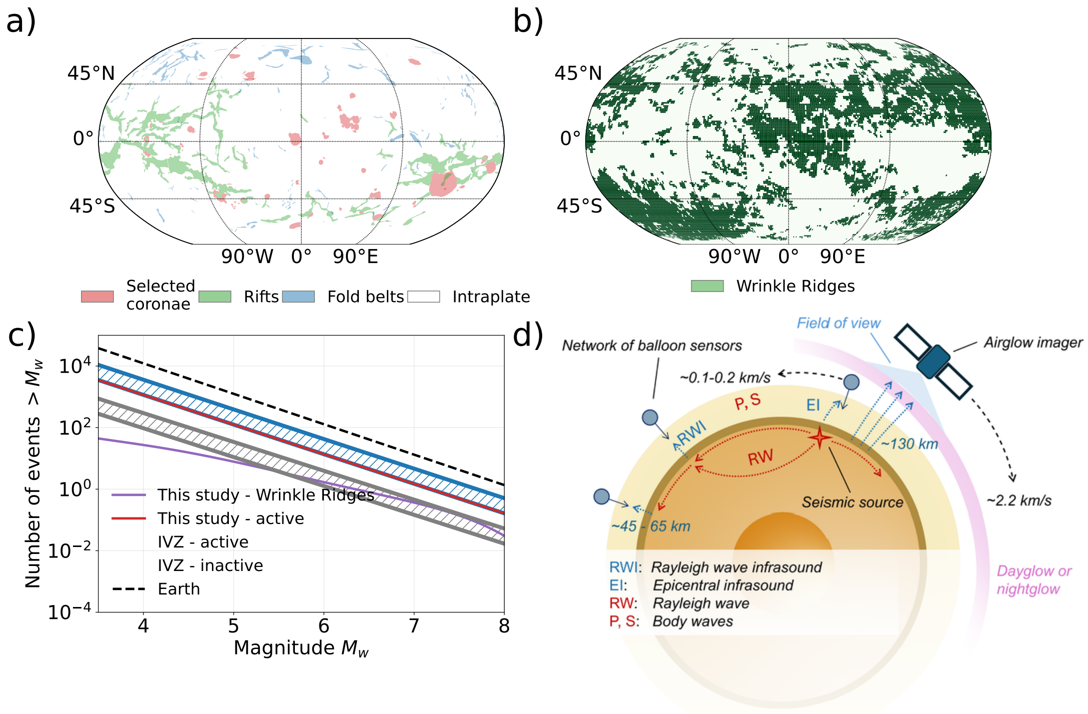

Figure 1. Seismicity and seismo-acoustic amplitude prediction models. (a) Tectonic settings on Venus as considered in *Van Zelst et al.* (2024a), which were based on global geologic maps by *Price and Suppe* (1995); *Price et al.* (1996), adapted with a down-selection of coronae based on recent suggestions of plume-induced crustal recycling at certain coronae (*Cascioli et al.*, 2025), (b) Global Wrinkle Ridge map from *Bilotti and Suppe* (1999) used in *Sabbeth et al.* (2023), (c) Seismicity estimates used in this study, and (d) schematic of the infrasound generation from seismic sources and detection by microbarometers onboard high-altitude balloon or in the airglow layers from an airglow imager.

using steps (1) and (2), and (4) we integrate the detection likelihood estimates computed at step (5) along a balloon trajectory.

2.1 Venus seismicity estimates

The spatial and temporal distribution of venusquakes is estimated from those used in *Van Zelst et al.* (2024a), with modifications based on predictions by *Gülcher et al.* (2025); *Cascioli et al.* (2025), and from *Sabbeth et al.* (2023), hereafter termed *Sabbeth et al.* (2023). *Van Zelst et al.* (2024a) assumed that the tectonic settings on Venus are seismically analogous to a set of specific terrestrial settings. The Venusian tectonic settings were classified into four classes: fold belts, rifts, coronae, and intraplate regions. The spatial distribution of the first three was based on global maps by *Price and Suppe* (1995); *Price et al.* (1996), while intraplate regions were defined as the areas outside these tectonic regions (Figure 1a). *Van Zelst et al.* (2024a) assumed these Venus settings to be seismically analogous to Earth's continental collision zones (fold belt analogue), continental rifts (rift analogue), subduction zones (corona analogue), and intraplate regions. With these Venusian tectonic regimes and Earth analogues, the number of venusquakes per year can then be estimated by scaling to Venus dimensions the number of seismic events in the corresponding tectonic settings on Earth. Scaling factors to account for Venus' dimensions were built on the basis of the ratio between seismogenic thickness on Venus and Earth (*Van Zelst et al.*, 2024a). That work considered three global seismicity scenarios: *Inactive*, *Low Activity*, and *High Activity*. In the *Inactive* scenario, the whole planet was assumed to have a background seismicity analogous to Earth's continental intraplate setting. In the other two scenarios, ridges, rifts, and intraplate regions were all considered seismically active, but in *Low Activity*, 27.8% of the total corona surface is active, whereas in *High Activity*, all coronae are active.

Because subduction zones are among Earth's most seismically active regions and produce the highest magnitude seismic events, the assumption linking corona activity to terrestrial subduction strongly influences *Van Zelst et al.* (2024a)'s conclusions. Especially the *High Activity* scenario results in a number of quakes per year on the same order as on Earth. Coronae are prevalent on Venus' surface, with 740 features recently cataloged (*Gülcher et al.*, 2025). Their tectonic formation has been attributed to various lithospheric responses above either buoyant or transient mantle plumes (e.g., *Grindrod and Hoogenboom*, 2006; *Dombard et al.*, 2007; *Gülcher et al.*, 2020; *Schools and Smrekar*, 2024) or above gravitational instabilities and lithospheric downwellings (*Hoogenboom and Houseman*, 2006; *Piskorz et al.*, 2014). Morphological evidence, analogue experiments, and thermo-mechanical modeling suggest that short-lived retreating subduction can occur along some coronae arcs (*Sandwell* *and Schubert*, 1992; *Davaille et al.*, 2017; *Gülcher et al.*, 2020, 2023; *Cascioli et al.*, 2025). However, it is unlikely that all coronae on Venus are analogues to active terrestrial subduction zones. To produce more realistic detectability estimates, we consider only *Van Zelst et al.* (2024a)'s *Inactive* and *Low Activity* scenarios. Furthermore, we refine the global distribution of coronae that are considered seismically active based on a recent study of their topographic and gravity signatures (*Cascioli et al.*, 2025), which proposes active plume-induced crustal recycling scenarios (subduction or lithospheric delamination) to occur on 34 coronae today (red features in Figure 1a). This refinement enables more meaningful spatially-dependent detectability estimates for these features. For simplicity, we keep the subduction analogue for these shortlisted coronae (see their distribution in red in Figure 1a).

Sabbeth et al. (2023), estimated the total seismic moment release on Venus based on mapped wrinkle ridges, which are compressive anticlines at the surface caused by blind thrust faults at depth (Figure 1b). They determined the total fault length from the global wrinkle ridge map produced by *Bilotti and Suppe* (1999). By assuming an average vertical slip extent, three tiers of segmentation, and a given deformation duration, *Sabbeth et al.* (2023) calculated the annual seismicity for these mapped wrinkle ridges. These estimates remain conservative for two reasons. First, the global wrinkle ridge map by *Bilotti and Suppe* (1999) maps global trends and overlooks many faults, thereby underestimating the total length of all wrinkle ridges on Venus (*Bethell et al.*, 2019). Second, *Sabbeth et al.* (2023) considered a 100M year deformation time and only three tiers of segmentation, producing a seismicity rate multiple orders of magnitude below Earth. This results in detection probabilities close to zero for a short mission duration at high noise levels. In order to produce more optimistic, yet realistic estimates, we introduced two modifications relative to *Sabbeth et al.* (2023)' work by considering a 1M year deformation time and five tiers of segmentation. The resulting seismicity remains low, within the same order of magnitude as the *inactive* (intraplate) scenario of *Van Zelst et al.* (2024a) (Figure 1c).

2.2 Seismo-acoustic modeling

Body and Rayleigh waves excited by venusquakes can couple to the atmosphere as both Epicentral infrasound and Rayleigh-wave infrasound which can propagate to high altitudes (Figure 1d). We model venusquake-induced infrasound in a given frequency range using an ensemble of possible seismic

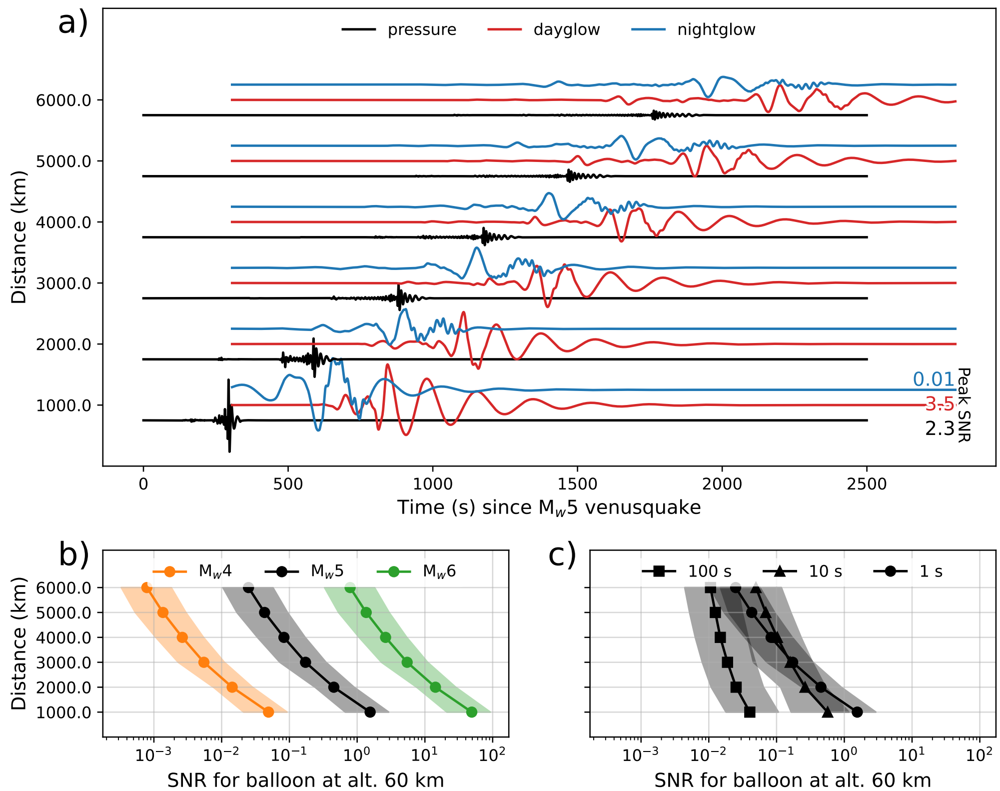

Figure 2. Seismo-acoustic amplitude based on the velocity model Cold100. (a) Simulated SNR timeseries, high pass filtered with the corner frequency 0.005 Hz for a M_w5 dip-slip venusquake (strike $\phi = 45°$, dip $\delta = 45°$, and rake $\lambda = 45°$) produced with a 5 s triangle source time function vs northward distance from the source for balloon pressure measurements at 60 km altitude (black), dayglow measurements (red), and nightglow (blue). (b) Median amplitude model for a venusquake of magnitude M_w4 (orange), M_w5 (black), and M_w6 (green) vs distance, computed for a variety of focal mechanisms, source depths, and strikes, along with the 0.25 and 0.75 quantiles (shaded regions). (c) Median amplitude model for a venusquake of magnitude M_w5 at period 100 s (circle), 10 s (triangle), and 1 s (square) vs distance, computed for a variety of focal mechanisms, source depths, and strikes, along with the 0.25 and 0.75 quantiles (shaded regions).

models, source location, and focal mechanisms through a three-step procedure: (1) We compute seismic Green's functions to determine ground vertical velocity at global scale using the QSSP method implemented in the `Pyrocko` Python package (*Heimann et al.*, 2019; *Wang et al.*, 2017); (2) We convert ground vertical velocities to ground pressure using a plane-wave assumption; and (3) We scale the ground pressure to account for the balloon altitude. Resulting waveforms can be bandpass filtered in a specific range to then extract the peak amplitude vs distance from the epicenter. The seismic modeling in step (1) allows us to predict the peak amplitude for any 1-D layered seismic model and any point moment tensor source while accounting for Venus' sphericity, which is important at global scales.

We build 1-D subsurface velocity models based on thermodynamic modeling and assuming three scenarios for the thermal profile and compositional changes with depth (see Appendix A for details). Our three scenarios represent plausible lithological end-members (e.g., basaltic crust and granitoid crust) for cold and hot geotherms inspired by the interior thermal structures of Venus in *Dumoulin et al.* (2017). This model, built with a cold geotherm and 50 km granitoid crust, leads to a clear crust-mantle boundary, similar to the Preliminary Reference Earth Model (PREM). However, the two other basalt-harzburgite hot models exhibit a thick low-velocity zone which creates large shadow zones that reduce the peak velocity amplitudes. By using 1-D layered models, we ignore mode- and wave-conversion in regions of rapid lateral seismic velocity variations (*Brissaud et al.*, 2020) and topographic scattering (*Brissaud et al.*, 2021). Such path effects could occur on Venus in regions of rapid change in crustal thickness, compositional change, and topography (e.g., *James et al.*, 2013). However, the best available crustal thickness models still only resolve smooth variations with dominant wavelength above 100 km, a scale too large to generate significant mode conversion.

The focal mechanism and focal depth are important parameters that control the amplitude in the far field. To account for these source- and path-effects and their uncertainties, we simulate Green's functions for all combinations of velocity models, at 20 different focal depths between 10 and 50 km, and considering strike-slip and dip-slip mechanisms. Our 50 km focal depth bound corresponds to the upper estimates of the seismogenic thickness on Venus (*Maia et al.*, 2024). Strike-slip and reverse-faulting events correspond to end members for peak vertical velocity at the surface, with strike-slip producing primarily horizontal motions and reverse, or normal, faults producing vertical motions. We then estimate the amplitude uncertainty based on the 0.25 and 0.75 quantiles of the peak amplitude realizations across all source and velocity model combinations. The amplitudes are not only focal mechanism dependent, but also frequency dependent, impacting both the source time function and path effects. Source time functions are intimately related to rupture processes, which are hard to define empirically. We therefore consider a Dirac source time function to avoid making additional assumptions about the physics of the source. To facilitate the detectability analysis across the full spectrum, we discretize the frequency into three logarithmically distributed bands such that at 100 s: (0, 0.05) Hz, at 10 s: (0.05, 0.22) Hz, and at 1 s: (0.22, 1) Hz.

We use a straightforward scaling to convert seismic amplitude v_z (m/s) into ground pressure p_s (Pa) in step (2), in the form $p_s = \rho_s c_s v_z$, where c_s (m/s) is the surface acoustic velocity, and ρ_s (kg/m^3) is the surface atmospheric density. In step (3), we scale the ground pressure amplitude to obtain the amplitude p_b at the balloon altitude using

$$p_b = \sqrt{\frac{\rho_b}{\rho_s}} p_s, \tag{1}$$

where ρ_b (kg/m^3) is the atmospheric density at the balloon altitude. Horizontal wind data are extracted on June 15, 2025, from the Venus Climate Database (VCD, *Lebonnois et al.*, 2010, 2016, 2022; *Martinez et al.*, 2023). We use a single density profile extracted at the equator and longitude 0 (SI 1). Although this scaling assumes a vertically propagating plane wave in a layered atmosphere, it provides an adequate amplitude approximation at large seismic wavelengths (*Macpherson et al.*, 2023; *Gerier et al.*, 2024). The impact of horizontal winds on acoustic amplitudes is assumed to be insignificant on this nearly-vertical infrasound propagation. Attenuation is typically low below 1 Hz on Venus up to and *Garcia et al.* (2024)). However, we consider attenuation for airglow computations at higher altitudes (see Appendix D). Finally, we ignore geometrical spreading, since seismic waves excite acoustic waves over large surface areas (*Brissaud et al.*, 2021).

Resulting pressure timeseries are dominated by surface waves at teleseismic distances (black line in Figure 2a). In contrast to pressure signals, dayglow and nightglow conversions lead to strong attenuation at high frequency (red and blue lines in Figure 2a). Note that volume emission rates peaking at lower altitude for the nightglow than dayglow, leads to earlier apparent arrival times in the nightglow. The balloon recorded SNR decreases with source distance, but the median SNR remains above 1 up to 6000 km range for a M$_w$6 venusquake (Figure 2b). We observe similar amplitudes at 1 and 10 s due to the presence of a strong crustal waveguide in the Cold100 model, leading to amplification of surface waves above 10 s, while longer periods consistently show lower amplitudes (Figure 2c). In contrast to Cold100, models built from hot geotherms that exhibit shadow zones lead to much lower SNR (SI 2). Note that the higher amplitude at short periods can also be explained by the use of a Dirac source time function to model venusquakes which is not a realistic representation of time-dependent rupturing behaviors observed in the far-field (*Aki*, 1972). Energy spectra of seismic waves in the far-field can be described using the notion of corner frequency beyond which energy steeply decreases capturing the impact of fault length and rupture velocity (*Brune*, 1970). Empirical relationships between source properties and corner frequency typically lead to much lower amplitudes at high frequencies and therefore smaller detection probabilities (SI 3). However, to avoid introducing a new set of parameters to capture the spectral decay of energy with frequency, we present results for a Dirac source in the remainder of this paper.

2.3 Venusquake detection probability framework

Determining venusquake detection probabilities bears similarities with building seismic hazard estimates, where the objective is to compute the probability that at least one earthquake generates ground motion exceeding a certain threshold (*Cornell*, 1968). Similarly, we want to determine the probability that at least one venusquake generates infrasound signals exceeding a certain Signal-to-Noise Ratio (SNR). This can therefore be described as a Poisson process assuming that the distribution of events over a given period of time follows a Poisson distribution in each tectonic region. We can then determine this detection probability as

$$\mathbb{P}(\mathrm{TL}/\sigma_n > d, M_{w,\min}, x^{\mathrm{obs}}_{\mathrm{lat,lon}}, t) \quad = \quad 1 - \exp\left[-\lambda(\mathrm{SNR} > d)t\right], \tag{2}$$

where $\mathbb{P}(\mathrm{SNR} > d, M_{w,\min}, x^{\mathrm{obs}}_{\mathrm{lat,lon}}, t)$ is the probability of observing at least one event with a Signal-to-Noise Ratio SNR $> d$ from a balloon location $x^{\mathrm{obs}}_{\mathrm{lat,lon}}$, for events with magnitude $M_w \geq M_{w,\min}$, with a balloon noise level σ_n (Pa), and a mission duration t (years), and where $\lambda(\mathrm{SNR} > d)$ is the rate of venusquakes producing signals with SNR exceeding d. In the rest of the manuscript, we will refer to the probability of observing at least one event with SNR exceeding d as the probability of detecting venusquakes. The rate λ depends on the yearly rate of venusquakes above a magnitude $M_{w,\min}$ in each tectonic region, expressed as $\lambda^{\mathrm{tec}}(M_w > M_{w,\min})$, as well as on the probability of detecting venusquakes from that region from the balloon location $\mathbb{P}(\mathrm{SNR} > d|\mathrm{tec})$, such that

$$\lambda(\mathrm{SNR} > d) = \sum_{\mathrm{tec}} \lambda^{\mathrm{tec}}(M_w > M_{w,\min})\mathbb{P}(\mathrm{SNR} > d|\mathrm{tec}). \tag{3}$$

The yearly rate of venusquakes is provided by the seismicity estimates for a given seismicity scenario (Section 2.1). As for the probability of detecting venusquakes from a given tectonic region $\mathbb{P}(\mathrm{SNR} > d|\mathrm{tec})$, it is obtained by integrating the probability of detecting a specific event over the range of possible magnitudes and distances from the source, which reads

$$\mathbb{P}(\mathrm{SNR} > d|\mathrm{tec}) = \int_{M_w = M_{w,\min}}^{M_{\max}} \int_{r=0}^{r_{\mathrm{Venus}}} \mathbb{P}(\mathrm{SNR} > d|M_w, r) f_M^{\mathrm{tec}}(M_w) f_R^{\mathrm{tec}}(r)\, dr\, dM_w, \tag{4}$$

where $\mathbb{P}(\mathrm{SNR} > d|M_w, r)$ is the probability of detecting venusquakes of a given magnitude M_w and from a distance r (km), r_{Venus} is the antipodal distance on Venus, i.e., maximum distance between two locations on Venus, $f_M^{\mathrm{tec}}(M_w)$ is the Probability Density Function (PDF) of an event with a specific magnitude M_w occurring in the tectonic region tec, and $f_R^{\mathrm{tec}}(r)$ is the PDF of an event occurring in the tectonic region tec at a distance r from the sensor location. These two PDFs read

$$\begin{aligned}
f_R^{\mathrm{tec}}(r, \mathbf{x}) &= \mathbb{P}(R < r) = \frac{\partial}{\partial r} \frac{\mathcal{S}(r, \mathbf{x}) \cap \mathcal{S}_{\mathrm{tec}}}{\mathcal{S}_{\mathrm{tec}}}, && (5)\\
\mathcal{S}(r, \mathbf{x}) &= \{P \in \mathrm{Venus} : \mathrm{dist}(P, \mathbf{x}) \leq r\}, && (6)\\
f_M^{\mathrm{tec}}(M_w) &= \mathbb{P}(M_w \geq M \geq M_{w,\min}) = -\frac{\partial}{\partial M_w} \frac{\lambda^{\mathrm{tec}}(M_w \geq M \geq M_{w,\min})}{\lambda^{\mathrm{tec}}(M \geq M_{w,\min})}, && (7)
\end{aligned}$$

where $\mathcal{S}_{\mathrm{tec}}$ is the surface area of tectonic region tec and $\mathcal{S}(r, \mathbf{x})$ is the projected circular surface area from balloon location $\mathbf{x}$ up to a distance r. Finally, the probability of detecting a specific venusquake $\mathbb{P}(\mathrm{SNR} > d|M_w, r)$ used in equation 4 corresponds to the probability of a venusquake to produce a signal with $\mathrm{SNR} > d$ integrated over all possible SNR values above d such that

$$\mathbb{P}(\mathrm{SNR} > d|M_w, r) = \int_{\mathrm{SNR}=d}^{\infty} f_{\mathrm{TL}}(\mathrm{SNR} = d, M_w, r)\, d\mathrm{SNR}, \tag{8}$$

where $f_{\mathrm{TL}}(\mathrm{SNR} = d, M_w, r)$ is the PDF of a specific venusquake to generate a signal with $\mathrm{SNR} = d$ where TL stands for Transmission Loss, i.e., the amplitude variations with distance, such that

$$f_{\mathrm{TL}}^{\mathrm{tec}}(\mathrm{SNR}, M_w, r) = \begin{cases} \mathcal{G}\left(\dfrac{\mathrm{TL}(M_w, r)}{\sigma_n}, \sigma_{\mathrm{TL},0.25}\right), & \text{if } \dfrac{\mathrm{TL}(M_w, r)}{\sigma_n} \leq \mathrm{SNR}, \\ \mathcal{G}\left(\dfrac{\mathrm{TL}(M_w, r)}{\sigma_n}, \sigma_{\mathrm{TL},0.75}\right), & \text{if } \dfrac{\mathrm{TL}(M_w, r)}{\sigma_n} > \mathrm{SNR}, \end{cases} \tag{9}$$

where $\mathrm{TL}(M_w, r)$, in Pa, is the maximum synthetic amplitude prediction for an event of magnitude M_w at a distance r from the source. The parameters $\sigma_{\mathrm{TL},0.25}$ and $\sigma_{\mathrm{TL},0.75}$, in Pa, are the predicted uncertainties, also called theory error, computed as the 0.25 and 0.75 quantiles of peak synthetic amplitudes for a range of focal depths and crustal thicknesses (Section 2.2), and $\mathcal{G}(\mu, \sigma)$ is the Gaussian distribution of mean μ and standard deviation σ. The noise level σ_n is still unconstrained for Venus conditions. We assume σ_n to be constant with frequency and on the same order of magnitude as the balloon noise recorded on Earth, which is $\sim 10^{-2}$ Pa (*Garcia et al.*, 2024). Yet, we do not need to recompute our detection probabilities for a different noise level since the probabilities are given in terms of SNR, i.e., a higher noise level simply corresponds to a lower SNR.

Several additional aspects need to be included to reflect the complexity and multi-instrument capabilities of future geophysical missions. Firstly, balloon sensors will be moving along Venusian winds. To include this effect, we simulate a trajectory from an initial drop off location, by considering a free floating balloon moving with horizontal winds at constant altitude. Detection probabilities computed at each location on Venus can then be integrated along the balloon trajectory to compute the final detection probability at the end of the mission (see Appendix B). Additionally, successful subsurface inversions require an accurate localization of seismic events, which can be achieved by combining observations from multiple locations. Therefore, assessing the detection of the same event across a balloon network is key. The balloon network detectability is estimated by varying the surface area $\mathcal{S}(r, \mathbf{x})$ in equation 7 and by considering the source-balloon distances as the maximum distance between sources across all balloons in the network (see Appendix C). Finally, airglow imagers will provide complementary acoustic wave observations, especially for large-magnitude events (*Garcia et al.*, 2024). We incorporate airglow-based SNR estimates into the detectability framework by including the airglow imager detection surface in the surface area $\mathcal{S}(r, \mathbf{x})$, to account for both the expected SNR in airglow data and the large field-of-view of airglow imagers (see Appendix D).

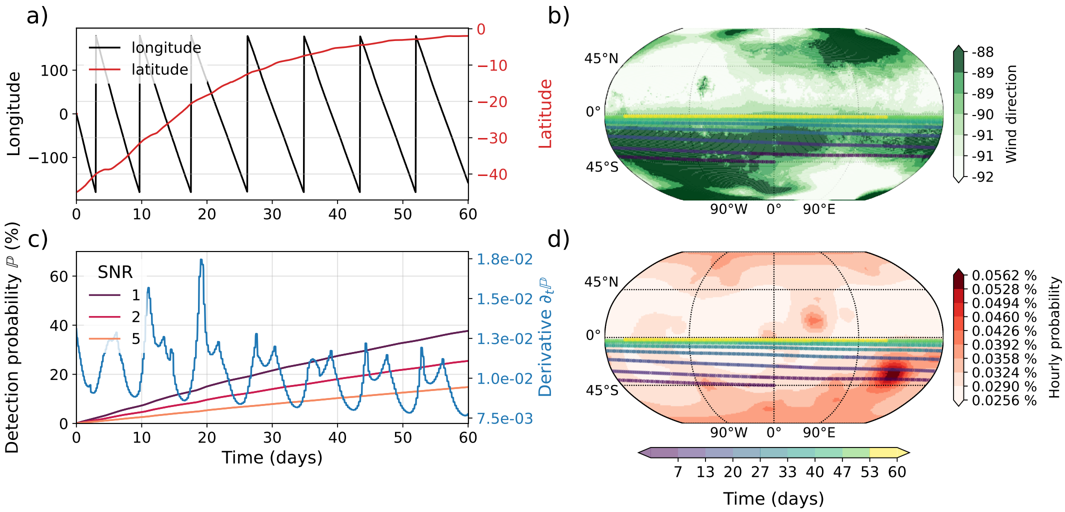

Figure 3. Tectonic event detection probability for a specific balloon flight analyzed at period 1 s for velocity model Cold100. (a) Balloon flight trajectories in longitude (black) or latitude (red) vs time. (b) Wind direction at 50 km altitude on Venus. The points show the balloon trajectory, color-coded by time. (c) Detection probability $\mathrm{SNR} = 1, 2, 5$ vs time (orange, red, purple lines) and time derivative of the detection probability for $\mathrm{SNR} = 1$ (blue line). (d) Hourly detection probability for $\mathrm{SNR} = 1$. The points show the balloon trajectory color-coded by time. The maps in (b,d) are in Robinson projection, centered at 0° longitude.

3 Tectonic event detectability

To illustrate both our trajectory and detection probability estimates, we first consider the detectability of events produced by the tectonic seismicity model, built from Earth catalogue scaling, from a single balloon being dropped off at an arbitrary location (0°E, 45°S). Trajectories for balloons flying at 50 km altitude are mostly westward (Figure 3a,b), which follows from the direction of the strong zonal winds in Venus' upper atmosphere. Interestingly, there is a small meridional wind component that causes the balloon to drift from high latitudes towards the equator (see SI 1). Similarly, balloons can get trapped in polar regions if dropped off within 5 degrees latitude from the poles, due to the strong polar vortex on Venus. Figure 3c shows detection probabilities that steadily increase with flight time to reach about 40% for SNR = 1 after 6 months. We observe peaks in the time derivative of the detection probability (blue line in Figure3c) corresponding to a sudden increase in detection likelihood as the balloon flies above the most active coronae (Figure 3a,d).

Because meridional wind components are mostly symmetrical around the equator, balloons consistently drift towards the equator for any drop-off latitude outside of polar regions (SI 4). However, in polar regions, balloons get trapped in the core of the zonal wind vortex. Yet, no matter the drop-off location and when considering long-duration flights, spatial heterogeneities in seismic activity (Figure 1c) do not significantly affect the final detection probability compared to a homogeneous global seismicity (SI 4). We obtain similar results at a period of 10 s, but the final detection probability drops at a period of 100 s due to lower amplitudes at low frequencies (SI 5). The presence of a strong crustal waveguide seems key to producing strong ground motions and detectable signals, as velocity models built from hotter thermal profiles lead to lower final detection probabilities (SI 6). Beyond tectonic seismicity, the lower moment rates for wrinkle ridges lead to significantly lower detection probabilities, at less than 10%, after a 6-month mission at 1 s (SI 7). Results are presented for the detection of at least one event, but the detection of several events could ensure more robustness in the inverted subsurface and source models. However, hourly detection probabilities lower than 50% for at least one event would drastically decrease for the detection of at least two events or more (SI 8).

Robust probability estimates should not be dependent on a specific balloon trajectory since drop-off locations are not constrained yet. We therefore simulated 6-month flights at three altitudes 50, 55, 60, and 65 km altitude, and from 750 different drop-off locations defined along a grid from latitudes 65°S to 65°N that excludes the polar latitudes. We then extracted median probabilities as well as quantiles 0.25 and 0.75 from this set of simulations. We computed statistics for three networks: (1) a single balloon, (2) a 3-balloon network dropped-off along the same latitude line with a maximum distance of 5000 km, and (3) a nightglow or dayglow imager. Due to the ground velocity increase with frequency, we observe a significantly higher final detectability level after 6 months (Figure 4a,b,c) at 1 s and 10 s (75%) than at 100 s (45%). We also observe up to 10% variability in detectability between the 0.25 and 0.75 quantiles, mainly due to different balloon flight altitudes and decreasing pressure with altitude. At 1 s, detection probabilities of the same event across the entire network

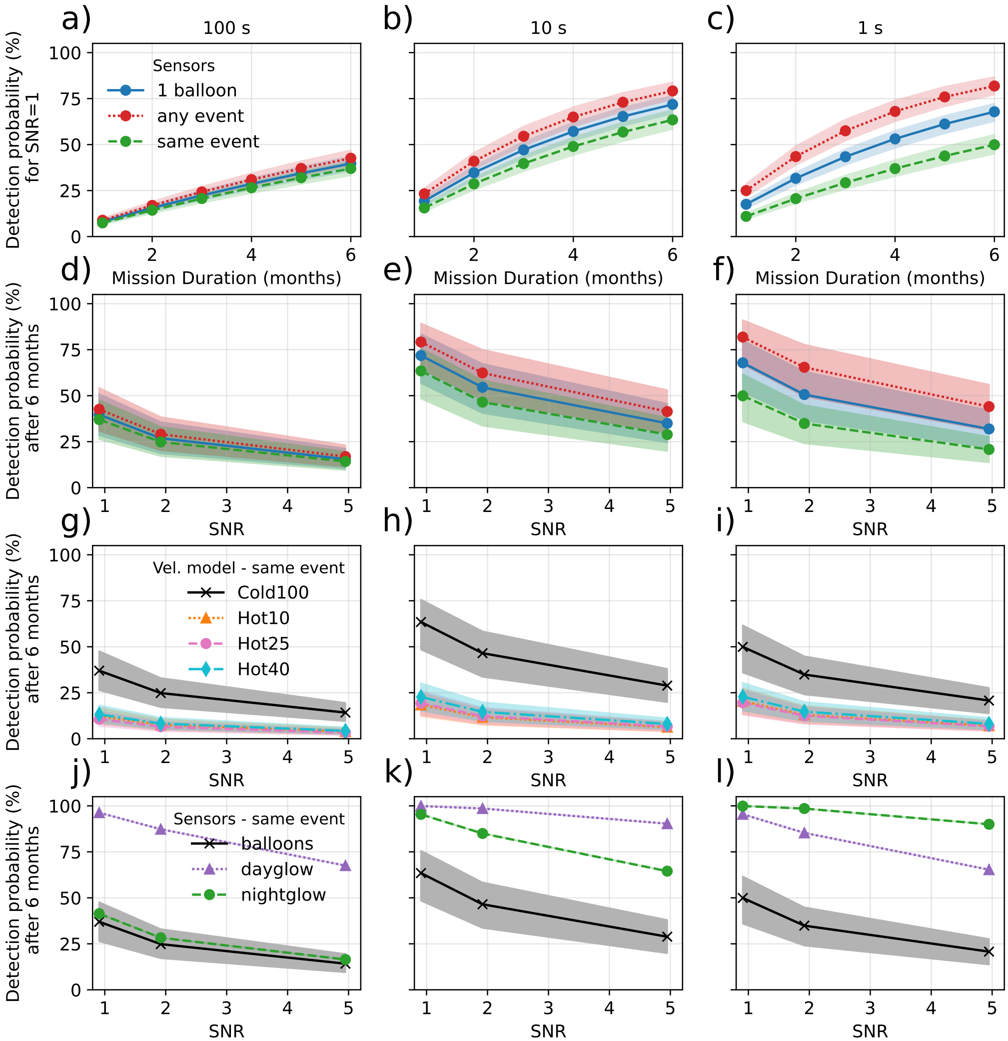

Figure 4. Tectonic event detection probability for balloon and airglow imager networks. Median detection probabilities (solid lines) along with the uncertainty (shaded regions), computed from the quantiles 0.25 to 0.75, for wave periods (a,d,g) 100 s, (b,e,h) 10 s, and (c,f,i) 1 s. For velocity model Cold100, (a,b,c) Detection probability vs mission duration for SNR = 1 and (d,e,f) Detection probability vs SNR over a 6-month long mission duration for a single balloon (1 balloon, blue circle) and for a 3-balloon network (any event and same event) averaged over all drop-off locations. The estimated balloon network detection probabilities are shown for the detection of a single event at all balloons across the network (same event, green circle) and for the detection of any event by at least one balloon in the network (any event, red circle). (g,h,i) Detection probability vs SNR over a 6-month mission for a balloon network for the velocity model Cold100 (black), Hot10 (orange), Hot25 (pink), and Hot40 (blue). (j,k,l) Detection probability vs SNR over a 6-month mission for velocity model Cold100 for an airglow imager probing the dayglow (purple triangle), nightglow (green circle), and a network of balloons (black crosses).

show a $\sim 30\%$ decrease (Figure 4c) compared to a single-balloon detection across a balloon network. The variability in detectability between network configurations decreases below $\sim 20\%$ for lower frequencies (Figure 4a,b). This behavior is likely due to the increased attenuation of high-frequency seismic motion, preventing its propagation at global scales. Detection probabilities decrease by about $25-35\%$ between $\mathrm{SNR}=1$ and $\mathrm{SNR}=5$ for all periods (Figure 4d,e,f). High SNR thresholds are generally reached for high-magnitude events which produce high-amplitude surface waves that travel globally. On the other hand, detecting any event from a network slightly increases the detection probability for low SNR thresholds. For longer periods, at 100 s, where predicted amplitudes are lower, both network and single balloon detection probabilities converge to lower values due to the absence of detectable signals at a global scale.

Detection probabilities are also highly dependent on the seismic velocity model as suggested by hourly detection probability maps (SI 6). Detectability levels for a 3-balloon network decrease significantly when using models built from hot geotherms by about 10 to 20% (Figure 4g,h,i). The presence of a strong crust-mantle interface in model Cold100 explains the larger final probabilities. Model Hot40 despite not exhibiting a large low-velocity zone in the upper mantle still produce detection probabilities on the same order as the other models built from hot geotherms. Airglow imagers typically yield a much higher detection probability than balloon networks: we estimate close to 100% at 100 s in the dayglow layer (Figure 4j,k,l). These high airglow detection probabilities are primarily driven by the large Field Of View (FOV) which is equivalent to a dense network of sensors. In contrast to balloon detectability, the low passing effects of the integration of volume emission rate perturbations in the airglow layer, lead to significant attenuation at 1 s. The thicker dayglow layer reduces the SNR even further at high frequency, compared to the nightglow layer (Figure 4l). Note that our results do not account for post-processing steps of airglow images that might increase the SNR, such as pixel and time binning (*Didion et al.*, 2018). We showed raw-image detections, but binning N pixels would increase the SNR by a factor N would also decrease the spatial resolution of each observation (*Kenda*, 2018). Comparing Figure 4d,e,f to Figure 4j,k,l, for low-SNR signals, the detectability of a single seismic event across both balloon and airglow sensors will therefore be mostly restricted by the detectability at the balloon sensors.

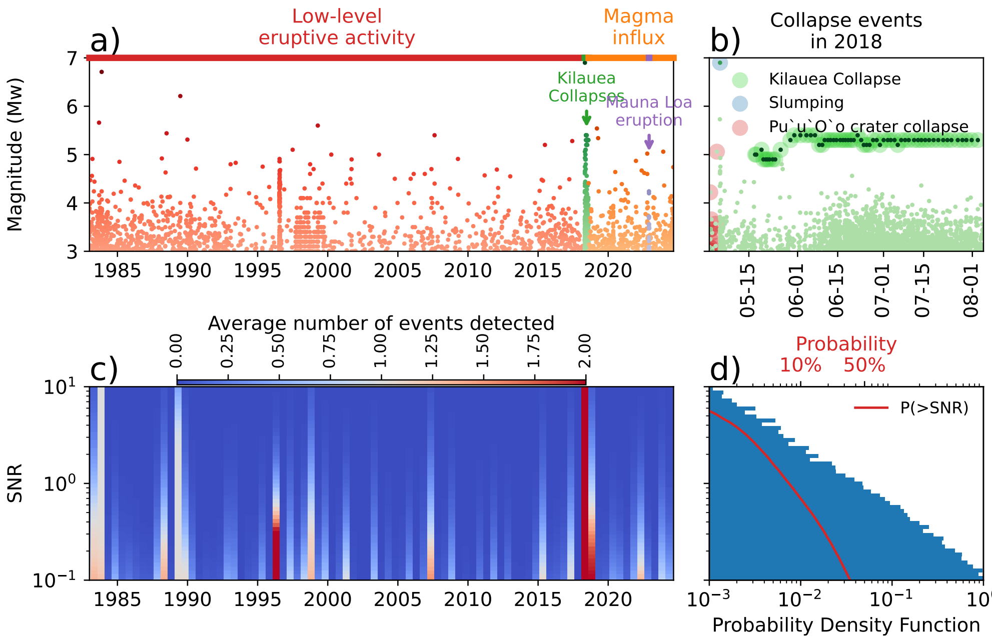

Figure 5. Volcanic sequence detection probability at 1 s for velocity model Cold100. (a) Seismic events extracted from the Hawaiian Volcano Observatory catalog in Hawai'i. (b) Seismic events from May to August 2018 showing the largest tectonic earthquake (Slumping), Pu'u 'O'o crater collapses, and Kilauea collapse events. (c) Simulated average number of detected events on Venus vs drop-off time and SNR across all drop-off locations. (d) Probability Density Function (blue histogram) and corresponding probability of observing a signal on Venus above a given SNR across the entire flight dataset ($P(>\mathrm{SNR})$, red).

4 Volcanic sequence detectability

In addition to major tectonic structures, Venus' surface is largely dominated by volcanic features (e.g., *Ghail et al.*, 2024), with at least tens of thousands of volcanoes, flows, and edifices identified across the planet *Hahn and Byrne* (2023); *Bickel et al.* (2025). Given that major terrestrial volcanoes are seismically active (*Phillipson et al.*, 2013), similar activity may also occur on Venus. The detection of volcanic seismicity on Venus would bring a better understanding of the driving processes behind the planet's volcanic activity, and provide additional constraints on its subsurface. Yet, the seismic potential of Venus volcanoes has been unexplored in previous work. Indeed, scaling Earth volcanism to Venus is a challenging task. Although some studies, such as *Byrne and Krishnamoorthy* (2022), have proposed a scaling of volcanic eruptions in terms of Volcanic Explosive Index (VEI), identifying the seismic contribution to the VEI requires several assumptions about volcanic source processes. Instead of introducing a large number of new scaling parameters to model volcanic seismicity, we opt to use seismic catalogs around well-instrumented Earth volcanoes as proxies for Venus volcanism.

There are several volcanoes on Venus with size and gravity signatures similar to hot-spot volcanoes on Hawaiʻi (*Herrick and Hensley*, 2023). In particular, *Herrick and Hensley* (2023) have confirmed the recent deformation of a volcanic vent related to the Maat Mons volcano in Alta Regio on Venus with dimensions of the same order of magnitude as the caldera collapse at Kilauea volcano, Hawaiʻi during the 2018 Kilauea eruption (*Neal et al.*, 2019). The authors have also speculated that some of the radar data near the event show a lava flow with, once again, similar dimensions to the Kilauea Puna eruption in Hawaiʻi. Moreover, gentle slopes in Hawaiʻi shield volcanoes show similarities with Venus volcanoes such as Idunn Mons (*D'Incecco et al.*, 2024). We therefore selected Mauna Loa and Kilauea calderas and their rift zones in Hawaiʻi as representative of typical seismicity in volcanic regions on Venus. This allows us to investigate variations of detectability not only in space but also in time for complex seismo-volcanic sequences, comprising explosive events, collapses, and deeper brittle failure events.

We extracted all seismic events above magnitude 3 in Hawaiʻi from the Hawaiian Volcano Observatory catalog (Figure 5a) since 1983 – the onset of the Puʻu ʻOʻo eruption. Several driving processes can explain the variability in seismicity since 2012 (Figure 5a,b):

- (2012–2018) low-level eruptive activity from long-lived Puʻu ʻOʻo eruption with infrequent surficial activity and slow-moving, small lava fronts;
- (May 1 – August 4 2018): Puʻu ʻOʻo crater floor collapse, causing a series of 62 $M_w > 5$ earthquakes at the summit;
- (May 4, 2018) M_w 6.9 earthquake, below Kilauea's south flank, caused by slumping of the volcanic pile;
- (November 27 – December 13 2022) First eruption at Mauna Loa following 38 years of quiescence;

– (2018–2024) Magma influx and small eruptions at Kilauea characterized by intermittent swarms of seismicity.

This dataset is particularly interesting as it includes a variety of source mechanisms such as collapse events and small lava flows, as have been observed on Venus. Here, we select the largest volcanic edifice on Venus, Maat Mons (8.7°N, 52.5°W), and assume that it produces the same seismicity as observed in Hawai'i. To provide meaningful detectability estimates, we simulate 14800 flights with drop off times every 6 months from 1983 to 2023 within 50 degrees latitude and 50 degrees longitude from the volcano location.

Considering that Maat Mons follows the same volcanic sequence as Hawai'i, the highest peak in number of events detected by the balloons, with a SNR above 2 would occur in 2018 when slumping happens, producing a M_w 6.9 earthquake, together with repeating collapse events around M_w 5 (Figure 5c). However, the average number of events detected across all drop-off locations remains below 1 across most years even for low SNR (Figure 5c). Only swarms of seismic activity with magnitudes above 4 can yield an average number of detections close to 1 (e.g., around 1996 and 2007). The probability of observing a signal with SNR > 1, integrated across all drop-off times, is around 8% for SNR > 1 and decreases to $2 - 3\%$ for SNR > 3 (Figure 5d). For SNR > 1, detection probabilities of volcanic seismicity from a single volcano $\mathbb{P}(V) \approx 8\%$ will therefore contribute with the tectonic event detection probability $\mathbb{P}(Q) \approx 65\%$ (Figure 4c) to the overall detection probability $\mathbb{P}(Q \cup V)$ such that $\mathbb{P}(Q \cup V) = 1 - [1 - \mathbb{P}(Q)][1 - \mathbb{P}(V)] \approx 3\%$ While this suggests a fairly minimal seismic contribution from volcanic seismicity to the detectability, we point out that volcanic events could occur around other volcanoes (*Byrne and Krishnamoorthy*, 2022) simultaneously. Once again, these balloon detection probabilities can be extrapolated to airglow measurements and other periods using the results described in Section 3. At 100 s, we observe a significant drop in detection probabilities with maximum probabilities around 2% for SNR > 1 (SI 9). On the other hand, the large FOV of dayglow measurements could lead to a increase in detection probabilities of about 25% at 1 s and more than 50% at larger periods (when comparing 1 balloon probabilities in Figure 4d,e,f and dayglow in Figure 4j,k,l).

5 Discussions and Limitations

Our results qualitatively agree with *Garcia et al.* (2024) in terms of detectability levels for long-duration missions. *Garcia et al.* (2024) predicted a detection of at least one seismic event above M_w 5 (with a 66% confidence level) from a balloon and for a 3-months long missions if 200 homogeneously distributed events occurred per year. Here, at 1 s, we reach the 66% confidence level for a 3- to 3.5-months long missions long mission as well (Figure 4c). This good agreement is explained by our tectonic event catalog, producing about 150 events per year (Figure 1c), i.e., on the same order as the minimum number of events predicted by *Garcia et al.* (2024). Our airglow detectability model produces probabilities larger than 66% for periods lower than 100 s for both dayglow and airglow implying that events could still be detected for a lower seismicity scenario. This is qualitatively consistent with the much smaller number of M_w 5 seismic events (about 6 in the nightglow and 4 in the dayglow) required for a detection in *Garcia et al.* (2024) compared to the number of events included in our catalog. However, our seismic amplitude prediction model differs strongly at low frequencies compared to *Garcia et al.* (2024). This is mainly due to the use of Dirac sources in the current study and limitations of the empirical model used by *Garcia et al.* (2024). On one hand, Dirac source time functions do not capture the true magnitude-corner frequency relationship observed for earthquakes (*Brune*, 1970). On the other hand, the magnitude-period-amplitude relationship used by *Garcia et al.* (2024) was initially designed for surface waves around $18 - 22$ s period, and is therefore not valid outside of this range.

The detection probability at given drop-off locations would increase under more active seismicity scenarios, such as global venusquake rates on the order of terrestrial earthquakes (SI 10). However, such high rates are unlikely due to the absence of plate tectonics and global subduction networks (*Ghail et al.*, 2024). Assuming all coronae to be active with subduction-like seismicity (as in *Van Zelst et al.*, 2024a) likewise contradicts previous analyses of the diverse corona morphologies (*Gülcher et al.*, 2025). On the other hand, lower seismicity levels, as proposed through *Sabbeth et al.* (2023)' wrinkle ridge model, result in small detection probabilities events even at low SNR (SI 7). This highlights the need for further constraints on Venus seismicity through geodynamic simulations along with noise modeling (e.g., *Gülcher et al.*, 2023). It should be noted that the wrinkle ridge seismicity estimates by *Sabbeth et al.* (2023) are likely conservative due to the use of a global map (*Bilotti and Suppe*, 1999), which does not resolve individual faults in detail. The tectonic scenarios considered here also exclude tesserae and other highly fractured terrains as seismically distinct from terrestrial intraplate settings.

In our probabilistic framework we also assumed that occurrence of tectonic venusquakes can be described by a Poisson process. This is typically not the case when extracting events from global catalogs, like in *Van Zelst et al.* (2024a), primarily due to time-dependent foreshock and aftershock sequences. Declustering techniques are generally applied on a local scale to identify aftershocks or foreshocks (*Gardner and Knopoff*, 1974) with, more recently, machine learning providing more generic approaches to a variety of earthquake catalogs (*Aden-Antoniów et al.*, 2022). However, applying such tools at a global scale is still challenging and will not correctly identify main shocks. Yet, as aftershocks typically decay quickly in magnitude with time, we can expect that the number of lower-magnitude venusquakes $< \mathrm{M}_w 5$ will decrease which won't significantly alter the detectability results presented here.

Seismicity is closely related to subsurface velocity structures. Our thermodynamical results indicate that in cases of high subsurface temperature profiles, large low-velocity zones are created, leading to smaller surface seismic motions and consequently reduced detection probabilities (Figure 4g,h,i). Large uncertainties in the subsurface models therefore become a challenge if the goal is to provide robust detection probability estimates. In particular, seismic attenuation is a key parameter that is difficult to constrain and future studies should revisit our mapping of AK135 quality factors to our Venus subsurface models. Beyond tectonic seismicity, global volcanic seismicity could enhance detection probabilities, despite small final detection probabilities for a single volcano, if high seismic activity occurs at multiple volcanoes, which can be expected considering the abundance of volcanoes on Venus' surface (*Hahn and Byrne*, 2023; *Bickel et al.*, 2025).

In addition to seismicity uncertainties, we made strong modeling assumptions to simplify the construction of our detection probability framework, which deserve further discussion to assess the robustness of our estimates: (1) A laterally homogeneous 1-D seismic model accurately represents Venus' interior, (2) The range of realistic Venus seismic velocities and attenuation parameters are known, (3) Venus' surface has no topography, (4) background VER models are time- and space-independent, (5) The deep atmosphere of Venus can be treated as an ideal gas, and (6) Horizontal winds are not time dependent. All six assumptions will have an impact on the predicted body and surface-wave amplitudes recorded from a balloon or airglow imager. Lateral variations in seismic velocity lead to amplification and de-amplification of certain frequencies as well as phase and surface wave mode conversions (*Brissaud et al.*, 2020). In particular, high crust-mantle impedance contrasts can promote the trapping of energy close to the surface. Additionally, strong scattering occurs as surface waves travel across topography, especially when the dominant wavelength of the topography is of the same order as the dominant wavelength of the surface wave. Beyond seismic velocity models, background VER are considered homogeneous both in space and time which is not valid (*Didion et al.*, 2018). VER amplitudes are expected to decrease away from the location of peak VER which would affect the conversion of acoustic waves into the airglow layer.

Furthermore, it is known that the CO_2 composing the deep atmosphere of Venus behaves more like a critical fluid than an ideal gas at its extreme temperature and pressure conditions. *Averbuch and Petculescu* (2025) showed that small variations in the sound velocity (about 5%) can be expected if applying a more general equation of state. Although this would not lead to significant changes in seismic-to-acoustic energy transmission, the authors also highlighted that at pressure and temperature closer to the critical point of CO_2, sound velocity could reach values close to zero, which would dramatically affect wave propagation within the first 10 km of Venus atmosphere. We should also mention that we did not consider direct infrasound from volcanic eruptions, which could be detected when a balloon is close to an active volcano. However, due to the lack of a strong waveguide in the Venus atmosphere (*Averbuch et al.*, 2023), direct infrasound detection would be limited to the vicinity of each volcanic source. Beyond wave modeling assumptions, we extracted wind profiles on June 15, 2025, to simulate balloon trajectories. However, the wind patterns fluctuate between local day and night, and building more realistic balloon trajectory models with 3-D wind models can be important to better understand the trajectories and the associated noise levels. Note that we considered period-independent noise levels which is not valid in practice as environmental sources, wind noise and vortex shedding (*Krishnamoorthy et al.*, 2020), balloon resonances (*Garcia et al.*, 2022), balloon scattering (*Godin*, 2024) will affect recordings in various frequency bands. SNR for the same input amplitude will therefore change with frequency. In particular, in polar regions near the eye of the polar vortex, we can expect much more instable wind patterns that would deteriorate SNRs despite our detection probability estimates converging to the same values for any balloon drop-off locations (SI 4).

6 Conclusions and Implication for future missions to Venus

Future joint balloon-airglow missions to Venus could provide an unprecedented level of detail on the subsurface. Our estimates for a 6-month mission suggest that detection probabilities peak at 10 s from $\sim 75\%$ for a single balloon, up to $\sim 65\%$ for the detection of the same event by a balloon network, and over $\sim 90\%$ for a detection by an airglow imager. We observe only minimal variations in the final detection probability over a 6-month mission when comparing the heterogeneous and homogeneous spatial distribution of venusquakes despite the hourly detection levels varying to 50% between the intraplate regions and the selected coronae (in Figure 1a). Therefore, the drop-off location of a balloon on Venus, provided that it is outside of the polar caps, has no significant impact on the final detection probability at the end of the mission. When considering other subsurface models built from hotter thermal profiles (see Appendix A), we observe much lower detection probabilities due to the absence of strong crustal waveguide (SI 6). Wrinkle Ridges seismicity releases significantly less energy in the atmosphere with about 4 to 5 times lower probabilities than for tectonic seismicity. Our estimates indicate that each swarm of volcanically-induced seismicity with magnitude above 4 (triggered by edifice collapse, slumping, or eruptions) could contribute an increase up to 3% in global seismicity for a single balloon mission. Note that our results are presented for venusquakes modeled with Dirac source time functions, for which we expect higher amplitude, and therefore larger final probability, at 1 s (e.g., 65% for a single balloon) compared to 100 s (e.g., 40% for a single balloon), after 6 months of flight.

The ultimate goal of future missions is the identification of body wave and/or surface wave arrivals to retrieve seismic velocities and/or seismic source properties. This requires the observation of the same event across at least three stations to allow for the accurate inversion of both source location and origin time along with subsurface velocities. Additionally, high-SNR signals are needed to obtain low uncertainties on arrival times or waveform shapes for body waves and surface waves in various frequency bands. Assuming that signals with $\mathrm{SNR} = 2$ would be enough to produce reasonable posterior distributions of seismic velocities, our results show a median detection probability after 6 months of 37% at 1 s for a 3-balloon network (Figure 4f) which is too low to ensure mission success. Note that we only considered a distribution of balloons along the same latitude line with a maximum distance of 5000 km and the impact of network geometry should be further investigated. Increasing the mission duration would steadily improve the detectability of high-SNR signals. Detectability vs mission duration follows a smooth second-order functional in each frequency band, allowing us to extrapolate that a 8 to 10 month mission would lead to the reference 66% confidence level used in *Garcia et al.* (2024).

Note that our work did not account for signal post-processing methods, which could be another way to increase the SNR. If each balloon can be equipped with several sensors along a tether (e.g., *Brissaud et al.*, 2021), beamforming techniques could also be applied to reduce incoherent noise. In contrast to balloon network detections, airglow detections consistently show detection probabilities above 66% for $\mathrm{SNR} = 2$ except in the nightglow at 100 s. Moreover, pixel and time binning could significantly increase the detectability by removing incoherent noise. However, the integration of volume emission rate perturbations within each airglow layer both reduces the amplitude and affects the phase. In particular, at high frequencies, accounting for acoustic-to-airglow transfer during the inversion of seismic dispersion from airglow data, could lead to large uncertainties in posterior distributions (*Kenda*, 2018), while balloon pressure data are not affected and produce a more direct mapping to seismic dispersion. Beyond subsurface velocity inversions, the event magnitude could be derived from the peak pressure amplitude and the source location, as peak pressure is directly related to peak ground velocity (*Macpherson et al.*, 2023). However, determining the moment rate and b-value on Venus will be challenging from a pure balloon network due to the need to detect a large number of events. For example, on Mars the moment rate estimated using 55 events still showed large uncertainties with values from 10^{15} to 10^{18} Nm/year (*Knapmeyer et al.*, 2023).

Our work further highlighted the potential of airglow missions to Venus, as well as joint balloon-airglow missions over 6 months to 1 year of observation for the detection of atmospheric signals to be used for retrieving subsurface velocities. In particular, joint detections across balloon networks and an airglow imager would allow to both capture accurately high and low frequencies to retrieve crustal and mantle properties. The current work also showed the importance of building realistic noise models in the Venus atmosphere since detection probabilities estimates vary by 50% when going from $\mathrm{SNR} = 1$ to $\mathrm{SNR} = 5$). Better constraining the seismic velocity prior models is also key, as it will strongly impact the seismic-to-acoustic energy coupling (SI 6). Future studies should investigate 3 main research topics: 1) assessing the impact of several modeling assumptions on wave amplitudes, 2) validating the inversion of subsurface velocities from balloon pressure data to assess the resulting uncertainties in terms of seismic velocities, and 3) better constraining the range of possible seismic subsurface models through thermodynamical simulations. This would allow us to further constrain the requirements in terms of SNR, and to refine the mission and instrument design requirements.

Acknowledgements

This work received support from the *Airborne Inversion of Rayleigh wave* (AIR) project, funded by the Research Council of Norway basic research program FRIPRO, Contract 335903, as well as NORSAR institute funding. We thank the Norwegian national e-infrastructure for computational science, Sigma2, for providing high-performance computational resources through the University of Oslo Project number NN8104K. A. G. acknowledges funding from the Center for Space and Habitability (CSH) at the University of Bern as well as NCCR PlanetS supported by the Swiss National Science Foundation under grant 51NF40_205606. J. M. J. thanks the JPL Strategic Research & Technology Development Program, "Venus Science Into the Next Decade" and the W. E. Keck Institute for Space Studies.

Author contributions

Conceptualization: Q. B., J. J., S. P. N.
Supervision: Q. B., J. J.
Methodology and Formal analysis: Q. B., C. K., J. J., A. G., M. F., J. W.
Investigation: Q. B., C. K., J. J., M. F., S. P. N., C. M. S., J. W.
Validation: Q. B., M. F.
Visualization: Q. B., C. K.
Writing – original draft: Q. B., C. K., A. G., J. W.
Writing – review and editing: Q. B., C. K., J. J., A. G., M. F., S. P. N., I. v. Z., R. G., C. M. S., J. W.

Competing interests

The authors declare that they have no competing interests.

Open Research

The detection probability framework will be made available at https://github.com/QuentinBrissaud/Venus_Detectability. The airglow amplitude prediction software will be made available at https://github.com/QuentinBrissaud/airglow_model. Tectonic setting shape files and moment rates are available at *Van Zelst et al.* (2024b). Wrinkle ridges spatial distribution and moment rates are available at *Sabbeth* (2023).

References

Aden-Antoniów, F., W. B. Frank, and L. Seydoux (2022), An adaptable random forest model for the declustering of earthquake catalogs, *Journal of Geophysical Research: Solid Earth*, *127*(2), e2021JB023,254.

Aki, K. (1972), Scaling law of earthquake source time-function, *Geophysical Journal International*, *31*(1-3), 3–25.

Armann, M., and P. J. Tackley (2012), Simulating the thermochemical magmatic and tectonic evolution of Venus's mantle and lithosphere: Two-dimensional models, *Journal of Geophysical Research*, *117*, E12,003, https://doi.org/10.1029/2012JE004231.

Averbuch, G., and A. Petculescu (2025), Calculating the acoustic and internal gravity wave dispersion relations in Venus's supercritical lower atmosphere, *The Journal of the Acoustical Society of America*, *157*(4), 3180–3191, https://doi.org/10.1121/10.0036505.

Averbuch, G., R. Houston, and A. Petculescu (2023), Seismo-acoustic coupling in the deep atmosphere of Venus, *The Journal of the Acoustical Society of America*, *153*(3), 1802–1810, https://doi.org/10.1121/10.0017428.

Ballmer, M. D., J. van Hunen, G. Ito, P. J. Tackley, and T. A. Bianco (2007), Non-hotspot volcano chains originating from small-scale sublithospheric convection, *Geophysical Research Letters*, *34*(23), https://doi.org/https://doi.org/10.1029/2007GL031636.

Bethell, E. M., R. E. Ernst, and C. Samson (2019), Geology of the Alpha Regio (V-32) quadrangle, Venus, *Journal of Maps*, *15*(2), 474–486, https://doi.org/10.1080/17445647.2019.1614489.

Bickel, V. T., C. L. Johnson, and M. B. Russell (2025), Revisiting volcanism on Venus with deep learning, in *Proceedings of the 56th Lunar and Planetary Science Conference*, Lunar and Planetary Institute, The Woodlands, Texas, USA, abstract 1387.

Bilotti, F., and J. Suppe (1999), The global distribution of wrinkle ridges on Venus, *Icarus*, *139*(1), 137–157, https://doi.org/10.1006/icar.1999.6092.

Brissaud, Q., D. C. Bowden, and V. C. Tsai (2020), Extension of the basin Rayleigh-wave amplification theory to include basin-edge effects, *Bulletin of the Seismological Society of America*, *110*(3), 1305–1322.

Brissaud, Q., S. Krishnamoorthy, J. M. Jackson, D. C. Bowman, A. Komjathy, J. A. Cutts, Z. Zhan, M. T. Pauken, J. S. Izraelevitz, and G. J. Walsh (2021), The first detection of an earthquake from a balloon using its acoustic signature, *Geophysical Research Letters*, *48*(12), e2021GL093,013, https://doi.org/10.1029/2021GL093013.

Brune, J. N. (1970), Tectonic stress and the spectra of seismic shear waves from earthquakes, *Journal of geophysical research*, *75*(26), 4997–5009, https://doi.org/10.1029/JB075i026p04997.

Byrne, P. K., and S. Krishnamoorthy (2022), Estimates on the frequency of volcanic eruptions on Venus, *Journal of Geophysical Research: Planets*, *127*(1), e2021JE007,040, https://doi.org/10.1029/2021JE007040.

Cascioli, G., A. J. P. Gülcher, E. Mazarico, and S. E. Smrekar (2025), A spectrum of tectonic processes at coronae on Venus revealed by gravity and topography, *Science Advances*, *11*(20), eadt5932, https://doi.org/10.1126/sciadv.adt5932.

Cornell, C. A. (1968), Engineering seismic risk analysis, *Bulletin of the seismological society of America*, *58*(5), 1583–1606, https://doi.org/10.1785/BSSA0580051583.

Davaille, A., S. E. Smrekar, and S. Tomlinson (2017), Experimental and observational evidence for plume-induced subduction on Venus, *Nature Geoscience*, *10*(5), 349–355, https://doi.org/10.1038/ngeo2928.

Didion, A., A. Komjathy, B. Sutin, B. Nakazono, A. Karp, M. Wallace, G. Lantoine, S. Krishnamoorthy, M. Rud, J. Cutts, et al. (2018), Remote sensing of Venusian seismic activity with a small spacecraft, the VAMOS mission concept, in *2018 IEEE aerospace conference*, pp. 1–14, IEEE, https://doi.org/10.1109/AERO.2018.8396447.

D'Incecco, P., J. Filiberto, J. Garvin, G. Arney, S. Getty, R. Ghail, L. M. Zelenyi, L. Zasova, M. Ivanov, D. Gorinov, et al. (2024), Mount Etna as a terrestrial laboratory to investigate recent volcanic activity on Venus by future missions: A comparison with Idunn Mons, Venus, *Icarus*, *411*, 115,959, https://doi.org/10.1016/j.icarus.2024.115959.

Dombard, A. J., C. L. Johnson, M. A. Richards, and S. C. Solomon (2007), A magmatic loading model for coronae on Venus, *Journal of Geophysical Research E: Planets*, *112*(4), 1–13, https://doi.org/10.1029/2006JE002731.

Dumoulin, C., G. Tobie, O. Verhoeven, P. Rosenblatt, and N. Rambaux (2017), Tidal constraints on the interior of Venus, *Journal of Geophysical Research: Planets*, *122*(6), 1338–1352, https://doi.org/10.1002/2016JE005249.

Dziewonski, A. M., and D. L. Anderson (1981), Preliminary Reference Earth Model, *Physics of the Earth and Planetary Interiors*, *25*(4), 297–356, https://doi.org/Doi 10.1016/0031-9201(81)90046-7.

Frost, D. J., and C. A. McCammon (2008), The redox state of earth's mantle, *Annu. Rev. Earth Planet. Sci.*, *36*(1), 389–420, https://doi.org/10.1146/annurev.earth.36.031207.124322.

Garcia, R. F., A. Klotz, A. Hertzog, R. Martin, S. Gérier, E. Kassarian, J. Bordereau, S. Venel, and D. Mimoun (2022), Infrasound from large earthquakes recorded on a network of balloons in the stratosphere, *Geophysical Research Letters*, *49*(15), e2022GL098,844, https://doi.org/10.1029/2022GL098844.

Garcia, R. F., I. Van Zelst, T. Kawamura, S. P. Näsholm, A. Horleston, S. Klaasen, M. Lefevre, C. M. Solberg, K. T. Smolinski, A.-C. Plesa, et al. (2024), Seismic wave detectability on Venus using ground deformation sensors, infrasound sensors on balloons and airglow imagers, *Earth and Space Science*, *11*(11), e2024EA003,670, https://doi.org/10.1029/2024EA003670.

Gardner, J., and L. Knopoff (1974), Is the sequence of earthquakes in Southern California, with aftershocks removed, Poissonian?, *Bulletin of the seismological society of America*, *64*(5), 1363–1367, https://doi.org/10.1785/BSSA0640051363.

Gerier, S., R. F. Garcia, R. Martin, and A. Hertzog (2024), Forward modeling of quake's infrasound recorded in the stratosphere on board balloon platforms, *Earth, Planets and Space*, *76*(1), 87, https://doi.org/10.1186/s40623-024-02030-7.

Ghail, R. C., S. E. Smrekar, T. Widemann, P. K. Byrne, A. J. Gülcher, J. G. O'Rourke, M. E. Borrelli, M. S. Gilmore, R. R. Herrick, M. A. Ivanov, et al. (2024), Volcanic and tectonic constraints on the evolution of Venus, *Space Science Reviews*, *220*(4), 36, https://doi.org/10.1007/s11214-024-01065-2.

Godin, O. A. (2024), Fidelity of infrasound measurements with balloon-borne sensors, *The Journal of the Acoustical Society of America*, *156*(6), 3909–3920, https://doi.org/10.1121/10.0034562.

Grand, S. P., and D. V. Helmberger (1984), Upper mantle shear structure of North America, *Geophysical Journal International*, *76*(2), 399–438, https://doi.org/10.1111/j.1365-246X.1984.tb05053.x.

Grindrod, P. M., and T. Hoogenboom (2006), Venus: The Corona Conundrum, *Astronomy & Geophysics*, *47*(3), 3.16–3.21, https://doi.org/10.1111/j.1468-4004.2006.47316.x.

Gülcher, A. J. P., T. V. Gerya, L. G. J. Montési, and J. Munch (2020), Corona structures driven by plume–lithosphere interactions and evidence for ongoing plume activity on Venus, *Nature Geoscience*, *13*(8), 547–554, https://doi.org/10.1038/s41561-020-0606-1.

Gülcher, A. J. P., T.-Y. Yu, and T. V. Gerya (2023), Tectono-magmatic evolution of asymmetric coronae on Venus: Topographic classification and 3D thermo-mechanical modeling, *Journal of Geophysical Research: Planets*, *128*(11), e2023JE007,978, https://doi.org/10.1029/2023JE007978.

Gülcher, A. J. P., L. Sabbeth, E. Stofan, and S. E. Smrekar (2025), Coronae on Venus: An updated global database and insights into morphology, spatial distribution, geological setting, and lithospheric properties, *Journal of Geophysical Research: Planets*, *130*(5), e2024JE008,749, https://doi.org/10.1029/2024JE008749.

Hahn, R. M., and P. K. Byrne (2023), A morphological and spatial analysis of volcanoes on Venus, *Journal of Geophysical Research: Planets*, *128*(4), e2023JE007,753, https://doi.org/10.1029/2023JE007753.

Hans Wedepohl, K. (1995), The composition of the continental crust, *Geochimica et Cosmochimica Acta*, *59*(7), 1217–1232, https://doi.org/https://doi.org/10.1016/0016-7037(95)00038-2.

Heimann, S., H. Vasyura-Bathke, H. Sudhaus, M. P. Isken, M. Kriegerowski, A. Steinberg, and T. Dahm (2019), A Python framework for efficient use of pre-computed Green's functions in seismological and other physical forward and inverse source problems, *Solid Earth*, *10*(6), 1921–1935.

Herrick, R. R., and S. Hensley (2023), Surface changes observed on a Venusian volcano during the Magellan mission, *Science*, *379*(6638), 1205–1208, https://doi.org/10.1126/science.abm7735.

Hoogenboom, T., and G. A. Houseman (2006), Rayleigh-Taylor instability as a mechanism for corona formation on Venus, *Icarus*, *180*(2), 292–307, https://doi.org/10.1016/j.icarus.2005.11.001.

Inchin, P., J. Snively, A. Williamson, D. Melgar, J. Aguilar Guerrero, and M. Zettergren (2020), Mesopause airglow disturbances driven by nonlinear infrasonic acoustic waves generated by large earthquakes, *Journal of Geophysical Research: Space Physics*, *125*(6), e2019JA027,628, https://doi.org/10.1029/2019JA027628.

James, P. B., M. T. Zuber, and R. J. Phillips (2013), Crustal thickness and support of topography on Venus, *Journal of Geophysical Research: Planets*, *118*(4), 859–875.

Kelemen, P. B., H. J. B. Dick, and J. E. Quick (1992), Formation of harzburgite by pervasive melt/rock reaction in the upper mantle, *Nature*, *358*(6388), 635–641, https://doi.org/10.1038/358635a0.

Kenda, B. (2018), Planetary applications of atmospheric seismology: Signals from the Martian turbulent atmosphere and observation perspectives in Venus' ionosphere, Master's thesis, Institut de Physique du Globe de Paris.

Kennett, B. L. N., E. R. Engdahl, and R. Buland (1995), Constraints on seismic velocities in the Earth from traveltimes, *Geophysical Journal International*, *122*(1), 108–124, https://doi.org/10.1111/j.1365-246X.1995.tb03540.x.

Knapmeyer, M., S. Stähler, A.-C. Plesa, S. Ceylan, C. Charalambous, J. Clinton, N. Dahmen, C. Durán, A. Horleston, T. Kawamura, et al. (2023), The global seismic moment rate of Mars after event S1222a, *Geophysical Research Letters*, *50*(7), e2022GL102,296, https://doi.org/10.1029/2022GL102296.

Kremic, T., R. Ghail, M. Gilmore, G. Hunter, W. Kiefer, S. Limaye, M. Pauken, C. Tolbert, and C. Wilson (2020), Long-duration Venus lander for seismic and atmospheric science, *Planetary and space science*, *190*, 104,961, https://doi.org/10.1016/j.pss.2020.104961.

Krishnamoorthy, S., V. H. Lai, A. Komjathy, M. T. Pauken, J. A. Cutts, R. F. Garcia, D. Mimoun, J. M. Jackson, D. C. Bowman, E. Kassarian, et al. (2019), Aerial seismology using balloon-based barometers, *IEEE transactions on geoscience and remote sensing*, *57*(12), 10,191–10,201, https://doi.org/10.1109/TGRS.2019.2931831.

Krishnamoorthy, S., D. C. Bowman, A. Komjathy, M. T. Pauken, and J. A. Cutts (2020), Origin and mitigation of wind noise on balloon-borne infrasound microbarometers, *The Journal of the Acoustical Society of America*, *148*(4), 2361–2370, https://doi.org/10.1121/10.0002356.

Lebonnois, S., F. Hourdin, V. Eymet, A. Crespin, R. Fournier, and F. Forget (2010), Superrotation of Venus' atmosphere analyzed with a full general circulation model, *Journal of Geophysical Research: Planets*, *115*(E6), https://doi.org/10.1029/2009JE003458.

Lebonnois, S., N. Sugimoto, and G. Gilli (2016), Wave analysis in the atmosphere of Venus below 100-km altitude, simulated by the LMD Venus GCM, *Icarus*, *278*, 38–51, https://doi.org/10.1016/j.icarus.2016.06.004.

Lebonnois, S., E. Millour, A. Martinez, T. Pierron, A. Bierjon, F. Forget, A. Spiga, J.-Y. Chaufray, F. Montmessin, F. Lefevre, and F. Cipriani (2022), The Venus Climate Database, in *Abstract B4.1-0013-22*, Athens, Greece, https://doi.org/10.5194/epsc2021-234.

Lognonné, P., W. B. Banerdt, J. Clinton, R. F. Garcia, D. Giardini, B. Knapmeyer-Endrun, M. Panning, and W. T. Pike (2023), Mars seismology, *Annual Review of Earth and Planetary Sciences*, *51*(1), 643–670, https://doi.org/10.1146/annurev-earth-031621-073318.

Macpherson, K. A., D. Fee, J. R. Colwell, and A. J. Witsil (2023), Using local infrasound to estimate seismic velocity and earthquake magnitudes, *Bulletin of the Seismological Society of America*, *113*(4), 1434–1456, https://doi.org/10.1785/0120220237.

Maia, J., A.-C. Plesa, I. Van Zelst, Q. Brissaud, B. De Toffoli, R. Garcia, R. Ghail, A. Gülcher, A. Horleston, T. Kawamura, et al. (2024), Constraining the seismogenic thickness of Venus, in *Europlanet Science Congress 2024*, vol. 17, pp. EPSC2024–915, A peer-reviewed journal paper version of this work has been accepted for publication in Journal of Geophysical Research: Planets, expected to become available in July 2025.

Martin, H. (1994), *The Archean grey gneisses and the genesis of continental crust*, vol. 11, pp. 205–259, Elsevier, https://doi.org/10.1016/S0166-2635(08)70224-X.

Martinez, A., S. Lebonnois, E. Millour, T. Pierron, E. Moisan, G. Gilli, and F. Lefèvre (2023), Exploring the variability of the Venusian thermosphere with the IPSL Venus GCM, *Icarus*, *389*, 115,272, https://doi.org/10.1016/j.icarus.2022.115272.

Morgan, J. W., and E. Anders (1980), Chemical composition of earth, venus, and mercury, *Proceedings of the National Academy of Sciences*, *77*(12), 6973–6977, https://doi.org/https://doi.org/10.1073/pnas.77.12.6973.

Neal, C. A., S. Brantley, L. Antolik, J. Babb, M. Burgess, K. Calles, M. Cappos, J. Chang, S. Conway, L. Desmither, et al. (2019), The 2018 rift eruption and summit collapse of Kīlauea Volcano, *Science*, *363*(6425), 367–374, https://doi.org/10.1126/science.aav7046.

Phillipson, G., R. Sobradelo, and J. Gottsmann (2013), Global volcanic unrest in the 21st century: An analysis of the first decade, *Journal of Volcanology and Geothermal Research*, *264*, 183–196, https://doi.org/10.1016/j.jvolgeores.2013.08.004.

Piskorz, D., L. T. Elkins-Tanton, and S. E. Smrekar (2014), Coronae formation on Venus via extension and lithospheric instability, *Journal of Geophysical Research: Planets*, *119*(12), 2568–2582, https://doi.org/10.1002/2014JE004636.

Poldervaart, A. (1955), *Chemistry of the earth's crust*, pp. 119–144.

Price, M., and J. Suppe (1995), Constraints on the resurfacing history of venus from the hypsometry and distribution of volcanism, tectonism, and impact craters, *Earth, Moon, and Planets*, *71*(1-2), 99–145, https://doi.org/10.1007/BF00612873.

Price, M. H., G. Watson, J. Suppe, and C. Brankman (1996), Dating volcanism and rifting on venus using impact crater densities, *Journal of Geophysical Research: Planets*, *101*(E2), 4657–4671, https://doi.org/10.1029/95JE03017.

Sabbeth, L. (2023), Estimated seismicity of venusian wrinkle ridges based on fault scaling relationships, https://doi.org/10.5281/zenodo.8011379.

Sabbeth, L., S. Smrekar, and J. Stock (2023), Estimated seismicity of Venusian wrinkle ridges based on fault scaling relationships, *Earth and Planetary Science Letters*, *619*, 118,308, https://doi.org/10.1016/j.epsl.2023.118308.

Sandwell, D. T., and G. Schubert (1992), Evidence for retrograde lithospheric subduction on Venus, *Science*, *257*(5071), 766–770, https://doi.org/10.1126/science.257.5071.766.

Schools, J., and S. Smrekar (2024), Formation of coronae topography and fractures via plume buoyancy and melting, *Earth and Planetary Science Letters*, *633*(118643), https://doi.org/10.1016/j.epsl.2024.118643.

Steinberger, B., S. C. Werner, and T. H. Torsvik (2010), Deep versus shallow origin of gravity anomalies, topography and volcanism on Earth, Venus and Mars, *Icarus*, *207*, 564–577, https://doi.org/10.1016/j.icarus.2009.12.025.

Stixrude, L., and C. Lithgow-Bertelloni (2005), Thermodynamics of mantle minerals – I. Physical properties, *Geophysical Journal International*, *162*(2), 610–632, https://doi.org/10.1111/j.1365-246X.2005.02642.x.

Stixrude, L., and C. Lithgow-Bertelloni (2011), Thermodynamics of mantle minerals – II. Phase equilibria, *Geophysical Journal International*, *184*(3), 1180–1213, https://doi.org/10.1111/j.1365-246X.2010.04890.x.

Stixrude, L., and C. Lithgow-Bertelloni (2024a), Thermodynamics of mantle minerals–iii: the role of iron, *Geophysical Journal International*, *237*(3), 1699–1733, https://doi.org/10.1093/gji/ggae126.

Stixrude, L., and C. Lithgow-Bertelloni (2024b), Thermodynanics of mantle minerals – III. The role of iron, *Geophysical Journal International*, https://doi.org/10.1093/gji/ggae126.

Sulcanese, D., G. Mitri, and M. Mastrogiuseppe (2024), Evidence of ongoing volcanic activity on Venus revealed by Magellan radar, *Nature Astronomy*, pp. 1–10, https://doi.org/10.1038/s41550-024-02272-1.

Sutin, B. M., J. Cutts, A. M. Didion, M. Drilleau, M. Grawe, J. Helbert, A. Karp, B. Kenda, A. Komjathy, S. Krishnamoorthy, et al. (2018), VAMOS: a SmallSat mission concept for remote sensing of Venusian seismic activity from orbit, in *Space telescopes and instrumentation 2018: optical, infrared, and millimeter wave*, vol. 10698, pp. 1651–1670, Spie, https://doi.org/10.1117/12.2309439.

Turcotte, D. L., and G. Schubert (2002), *Geodynamics*, 2 ed., Cambridge University Press, Cambridge, https://doi.org/DOI: 10.1017/CBO9780511807442.

Van Zelst, I., J. S. Maia, A.-C. Plesa, R. Ghail, and M. Spühler (2024a), Estimates on the possible annual seismicity of Venus, *Journal of Geophysical Research: Planets*, *129*(7), e2023JE008,048, https://doi.org/10.1029/2023JE008048.

Van Zelst, I., J. Maia, A.-C. Plesa, R. Ghail, and M. Spühler (2024b), Data & scripts - estimates on the possible annual seismicity of venus, https://doi.org/10.5281/zenodo.12166635.

Wang, R., S. Heimann, Y. Zhang, H. Wang, and T. Dahm (2017), Complete synthetic seismograms based on a spherical self-gravitating Earth model with an atmosphere–ocean–mantle–core structure, *Geophysical Journal International*, *210*(3), 1739–1764, https://doi.org/10.1093/gji/ggx259.

Widemann, T., S. E. Smrekar, J. B. Garvin, A. G. Straume-Lindner, A. C. Ocampo, M. D. Schulte, T. Voirin, S. Hensley, M. D. Dyar, J. L. Whitten, et al. (2023), Venus evolution through time: key science questions, selected mission concepts and future investigations, *Space Science Reviews*, *219*(7), 56, https://doi.org/10.1007/s11214-023-00992-w.

Workman, R. K., and S. R. Hart (2005), Major and trace element composition of the depleted MORB mantle (DMM), *Earth and Planetary Science Letters*, *231*(1), 53–72, https://doi.org/10.1016/j.epsl.2004.12.005.

Appendix A: Subsurface velocity models

As Venus' present-day interior thermal and lithological structure remains poorly constrained (e.g., *James et al.*, 2013; *Dumoulin et al.*, 2017), we consider several 1-D layered models of Venus' upper 300 km elastic structure that represent plausible lithological end-members. These profiles are generated by extrapolating Earth's shallow lithological layers to conditions envisioned for Venus' thermal and compositional state (Figure A1a,b). The thermal profiles considered correspond to the upper 300 km of two end-member geotherms for Venus' interior, labeled M1 to M3 and corresponding to "hot" and "cold" scenarios, based on *Dumoulin et al.* (2017) and originally derived from *Steinberger et al.* (2010) and *Armann and Tackley* (2012) (Figure A1c). These profiles differ in mantle potential temperature (1600 K vs. 1900 K) and adiabatic gradient (0.3 K/km vs. 0.5 K/km). The resulting 1-D background seismic models used to compute the Green's functions in step (1) are shown in Figure A1d,e,f.

To refine the uppermost lithospheric thermal structure, we employ a half-space cooling model (*Turcotte and Schubert*, 2002), commonly used in geodynamic modeling (e.g., *Gülcher et al.*, 2020).

This model incorporates the relevant potential temperatures and adiabatic gradients along with different lithospheric ages: 10 and 25 Myr for the two "hot" profiles, and 100 Myr for the "cold" profile. These thermal profiles are combined with several 1-D internal layering profiles (Figure A1a). This layering is based on an underlying mineralogical model with depth-dependent mineral fractions that include ferric iron, computed using a two-step approach. First, we assume four distinct lithological end-members that could plausibly exist within Venus' crust-mantle system: granitoid crust, basaltic crust, harzburgite-depleted mantle lithosphere, and the primitive mantle. The detailed chemical compositions of these end-members are shown in Figure A1b. We adopt basalt and harzburgite models from *Stixrude and Lithgow-Bertelloni* (2024a), a granitoid model representative of Archean-type continental crust from *Martin* (1994), and a primitive mantle composition estimated from solar nebula fractionation processes (*Morgan and Anders*, 1980; *Dumoulin et al.*, 2017). We consider four thermomechanical structures in this study, see Figure A1c,d,e,f.

Our hottest and thinnest lithosphere end-member, M1-Hot10, features a thin basaltic crust over a harzburgite-depleted mantle lithosphere and primitive mantle, combined with the hottest geotherm. This configuration is representative of Venusian regions with lithospheric and crustal thinning, such as rift zones and some coronae (e.g., *Sabbeth et al.*, 2023). The second structure, M2-Hot25, includes a slightly thicker basaltic crust (10 km) over a more substantial harzburgite-depleted lithosphere, underlain by the primitive mantle, combined with a hot but somewhat cooler lithosphere—representative of volcanic plains regions (e.g., *James et al.*, 2013). The chemical boundary between the harzburgite lithosphere and the underlying primitive mantle may be blurred because of the effects of graded melting (e.g., *Kelemen et al.*, 1992) and small scale convection in the asthenosphere (e.g., *Ballmer et al.*, 2007). To account for this, we proposed an additional end-member M2-Hot40, derived from M2-Hot25, in which the harzburgite is thoroughly mixed with the primitive mantle. As an opposing end-member to basaltic crust models, we consider a thick granitoid crust over a cold lithosphere (M3-Cold100), as suggested for crustal plateau regions (e.g., *Poldervaart*, 1955; *Hans Wedepohl*, 1995). The density and elastic properties of these models are calculated using the temperature and pressure conditions derived from the chosen geotherms (Figure A1c). For each lithological composition and its corresponding pressure-temperature path, we use the thermodynamic software `HeFESTo` (*Stixrude and Lithgow-Bertelloni*, 2005; *Workman and Hart*, 2005; *Stixrude and Lithgow-Bertelloni*, 2011, 2024a) to compute elastic properties. Unlike many previous models that only consider ferrous iron, our model incorporates ferric iron. `HeFESTo` determines the phase equilibrium of a specified set of candidate mineral species by minimizing the Gibbs free energy. Based on this equilibrium and a consistent thermodynamic framework, it calculates the corresponding thermodynamic quantities of the assemblage at the specified conditions. In this study, we use the default ambient-condition mantle species dataset provided with `HeFESTo`.

Appendix B: Accounting for balloon trajectories

To account for the motion of our observation point, i.e., the balloon motion, we compute flight trajectories $\mathbf{x}_{lat_0,lon_0,t_{\max}}$ up to a flight time $t_{\max}$ by considering a free floating balloon at a constant altitude z_b freely moving with Venus' horizontal winds, such that

$$\begin{aligned}\mathbf{x}_t^{\text{obs}} &= \mathbf{x}_{t-\Delta t}^{\text{obs}} + \mathbf{v}_{wind}(\mathbf{x}_{t-\Delta t}^{\text{obs}})\Delta t \\ \mathbf{x}_0^{\text{obs}} &= \mathbf{x}_{lat_0,lon_0},\end{aligned} \tag{B1}$$

where $\mathbf{x}_t^{\text{obs}}$ is the balloon location at time t, Δt in s is the time step, $\mathbf{v}_{wind}(\mathbf{x}^{\text{obs}})$ is the horizontal wind vector at location $\mathbf{x}^{\text{obs}}$, and $\mathbf{x}_{lat_0,lon_0}$ is the origin location of the balloon. We can then compute the detection probability for a given balloon flight $\mathbb{P}(\text{SNR} > d, M_{w,\min}, \mathbf{x}_{lat_0,lon_0}, t_{\max}, \sigma_n)$, up to a time $t_{\max}$ and from an origin location $\mathbf{x}_{lat_0,lon_0}$, by determining the probability of not detecting *any* event at each location along the balloon trajectory $\mathbf{t}$ such that,

885 $$\mathbb{P}(\text{SNR} > d, M_{w,\min}, \mathbf{x}_{lat_0,lon_0}, t_{\max}, \sigma_n) = 1 - \prod_{i=0}^{N=\frac{t_{\max}}{\Delta t}} \left[1 - \mathbb{P}(\text{SNR} > d, M_{w,\min}, x_{i\Delta t}^{\text{obs}}, \sigma_n, \Delta t)\right], \tag{B2}$$

where $\mathbb{P}(\text{SNR} > d, M_{w,\min}, x_t^{\text{obs}}, \sigma_n, \Delta t)$ is given by equation (2) and Δt (years) is the time step.

Appendix C: Incorporating a balloon network

We have so far described the detection probability for a single balloon, but future missions will need to deploy several balloons to (1) maximize the detection likelihood of venusquakes and (2) accurately

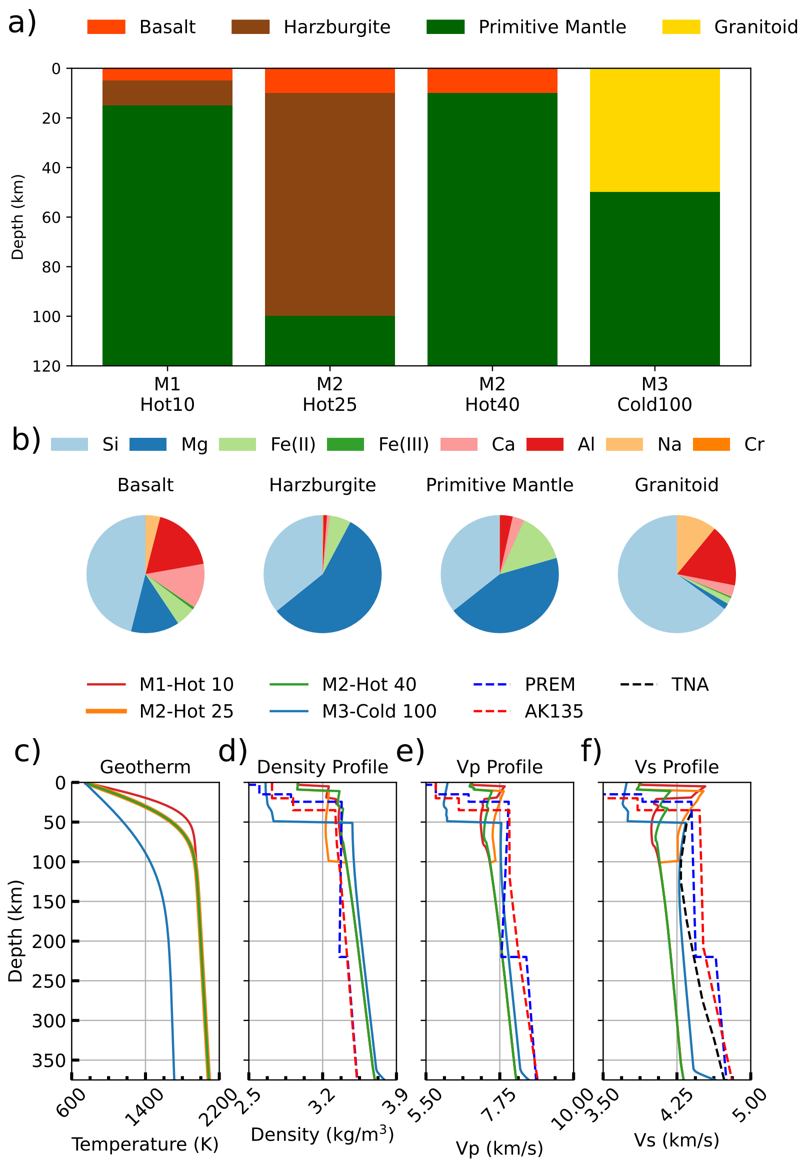

Figure A1. Construction of thermodynamically stable seismic velocity models. (a) 1-D layered thermochemical models M1 to M3, formulated by layered lithology and geotherms. We consider at most 3 layers representing crust, mantle lithosphere, and sub-lithosphere mantle. (b) Lithological end-member compositions in molar percentages. Basalt, harzburgite, are from *Stixrude and Lithgow-Bertelloni* (2024b), after *Workman and Hart* (2005) and *Frost and McCammon* (2008), and granitoid is modified from (*Martin*, 1994). Primitive mantle composition is modified from *Dumoulin et al.* (2017). (cdef) 1-D layered thermochemical models: M1 to M3, and their: (c) geotherm; (d) density; (e) P-wave velocity; (f) S-wave velocity. Elastic properties derived from Earth's global reference models, PREM (*Dziewonski and Anderson*, 1981) and ak135 (*Kennett et al.*, 1995), are shown in (cdef). A regional shear wave model TNA for western North America (*Grand and Helmberger*, 1984), is also included for comparison.

retrieve their location and timing. To ensure the detection, i.e., observation of a signal above an SNR threshold, of the same event across the entire network, the amplitude of the signal at the balloon furthest from the source needs to be larger than the SNR threshold. Therefore, to determine the detection likelihood we can simply replace the station-to-venusquake distance r in equation (4) by the maximum distance between a venusquake and all balloons such that

$$\mathbb{P}(\mathrm{SNR} > d, \mathbf{x}^b|\mathrm{tec}) = \int_{M_w=M_{w,\min}}^{M_{\max}} \int_{r=0}^{r_{\mathrm{Venus}}} \mathbb{P}(\mathrm{SNR} > d|M_w, r) f_M^{\mathrm{tec}}(M_w) f_{R,\mathrm{network}}^{\mathrm{tec}}(r, \mathbf{x}^b) dr dM_w, \tag{C1}$$

where $(\mathbf{x}_n^b)_{n=1,N_{balloons}}$ are the coordinates of each of the $N_{balloons}$ balloons, and $f_{R,\mathrm{network}}^{\mathrm{tec}}(r, \mathbf{x}^b)$ is the PDF of an event occurring in the tectonic region tec at a distance r from the furthest sensor location defined by

$$f_{R,\mathrm{network}}^{\mathrm{tec}}(r, \mathbf{x}^b) = \mathbb{P}(R < r) = \frac{\partial}{\partial r} \frac{\mathcal{S}_{\mathrm{network}}(r, \mathbf{x}^b) \cap S_{\mathrm{tec}}}{S_{\mathrm{tec}}}, \tag{C2}$$

$$\mathcal{S}_{\mathrm{network}}(r) = \left\{P \in \mathrm{Venus} : \max\left(\mathrm{dist}(P, \mathbf{x}_1^b), \mathrm{dist}(P, \mathbf{x}_2^b), \ldots, \mathrm{dist}(P, \mathbf{x}_N^b)\right) \leq r\right\}. \tag{C3}$$

While the detection of the same event across the entire network is valuable for inversion purposes, determining the detection probability of any events with a network would give us insights on the advantages of deploying a network vs a single sensor to improve venusquake sensitivity. The detection of any events can be simply computed by replacing the maximum operator in equation (C3) by a minimum operator such that

$$\mathcal{S}_{\mathrm{network}}^{\mathrm{any\ event}}(r) = \left\{P \in \mathrm{Venus} : \min\left(\mathrm{dist}(P, \mathbf{x}_1^b), \mathrm{dist}(P, \mathbf{x}_2^b), \ldots, \mathrm{dist}(P, \mathbf{x}_N^b)\right) \leq r\right\}. \tag{C4}$$

Appendix D: Incorporating airglow measurements

Airglow imagers onboard orbiters could provide a unique or complementary set of measurements together with a balloon network. Synthetic modeling shows that the perturbation of airglow emission by large earthquakes could be detectable on Earth (*Inchin et al.*, 2020) and previous mission concepts have highlighted the potential for seismic-induced variations of the 1.27 μm nightglow and the 4.28 μm dayglow on Venus (*Didion et al.*, 2018; *Sutin et al.*, 2018). *Garcia et al.* (2024) provided airglow detectability estimates but made several assumptions about the underlying physics: (1) amplitudes can be determined from an empirical magnitude-to-amplitude equation, (2) the frequency dependence of the acoustic to airglow coupling can be neglected despite having a strong influence on integrated airglow signals (*Kenda*, 2018, Section 4.3), (3) shot noise in photon inputs was ignored while it heavily corrupts airglow images especially at 1.27 μm (*Kenda*, 2018, Section 4.4), and (4) spatial and temporal pixel binning was not considered despite being key to greatly enhance SNR. Finally, *Garcia et al.* (2024) did not investigate the detectability of the same event through a hybrid balloon-airglow network.

Kenda (2018) summarized the wave equations required to approximate the neutral-to-airglow coupling by assuming a purely vertically plane wave $v_z(z,t)$ (Section 4.3 *Kenda*, 2018). Their derivation is presented in SI 11. However, these equations did not include the frequency-dependent attenuation terms. In order to account for frequency-dependent attenuation, we integrate the absorption coefficient α and bottom ground velocity along a vertical path such that

$$\mathcal{F}\left[v_z(M_w,r,z,t)\right] = \mathcal{F}\left[v_z(M_w,r,0,\tilde{t}(t,z))\right] A(z,f), \tag{D1}$$

$$\tilde{t}(t,z) = t - \int_z dz/c(z), \tag{D2}$$

$$A(z,f) = \left[\frac{\rho(0)}{\rho(z)}\right]^{1/2} e^{-\int_z \alpha(f,z)dz}, \tag{D3}$$

where $\mathcal{F}$ is the Fourier transform, and $v_z(M_w,r,0,t)$ (m/s) is the ground velocity perturbation, for an event at a distance r and a magnitude M_w, computed with scaled seismic Green's functions as defined in Section 2.2 such that $v_{z,0} = \rho_b c_b p_b$. $A(z,f)$ is the amplification due to density decrease with altitude and attenuation effects. The Airglow Signal-to-Noise Ratio SNR$_{airglow}$ is then defined as the ratio of emitted photons to shot noise $\sigma_{shot\ noise}$. Emitted photons can be computed as a disturbance over the total number of photons emitted by a given layer P where the disturbance is given by the Volume Emission Rate (VER) perturbation over the background VER produced by acoustic waves described by

$$\mathrm{SNR}_{\mathrm{airglow}}(M_w,r) = \frac{\max_t\left[I(M_w,r,t)\right]}{\int\limits_{z_{\min}}^{z_{\max}} \mathrm{VER}(z)\; dz}\frac{P}{\sigma_{\text{shot noise}}} \tag{D4}$$

$$I(M_w,r,t) = \int\limits_{z_{\min}}^{z_{\max}} \delta\mathrm{VER}(M_w,r,z,t)\; dz, \tag{D5}$$

where the shot noise is assumed to be the dominant source of noise and is given by $\sigma_{shot\ noise} \approx \sqrt{P}$, the total numbers of photons in each layer are $P^{1.27} \approx 2e^4$, $P^{4.28} \approx 3.5e^5$, and δVER is given for 1.27 μm and 4.28 μm layers as

$$\delta\mathrm{VER}^{1.27}(M_w,r,z,t) = \mathcal{F}^{-1}\left[-\frac{\tau}{1+i\omega\tau}\mathcal{F}\left[\mathrm{VER}(z)\frac{\partial}{\partial z}v_z(M_w,r,z,t)\right]\right] \tag{D6}$$

$$\delta\mathrm{VER}^{4.28}(M_w,r,z,t) = \alpha(\gamma-1)\mathrm{T}(z)\mathrm{VER}(z)\left[\frac{\partial}{\partial z}u_z(M_w,r,z,t)+\frac{u_z(M_w,r,z,t)}{\rho_0(z)}\frac{\partial}{\partial z}\rho_0(z)\right] \tag{D7}$$

$$-u_z(M_w,r,z,t)\frac{\partial}{\partial z}\mathrm{VER}(z), \tag{D8}$$

where $\mathcal{F}^{-1}$ is the inverse Fourier transforms, $\tau = 4460$ s (*Kenda*, 2018, Section 4.3) is the photon radiative lifetime, $\omega = 2\pi f$ is the pulsation, $\alpha = 1\%$ is the airglow sensitivity to a temperature perturbation in the 4.28 μm layer, and $u(z,t)$ (m) is the displacement perturbation defined by equation (D3).

To incorporate airglow data within the same probabilistic framework, we re-scaled the surface area defined by source-station distances in equation 7 to account for both the higher altitude of propagation to the airglow layer as well as the conversion from acoustic wave to airglow. Scaled source-receiver distances $R = r + \tilde{r}$ for airglow can be found by solving for $\tilde{r}$, i.e., the horizontal distance parameter for which pressure SNR at the balloon altitude and at a distance r is equal to airglow SNR at a distance $r + \tilde{r}$:

$$\frac{\mathrm{TL}(M_w, R = r + \tilde{r})}{\sigma_n} = \beta\mathrm{SNR}_{airglow}(M_w,r), \tag{D9}$$

where β is the pixel binning factor. One of the main advantages of airglow imagers is the large Field Of View (FOV), with a 60 degrees radius centered around the satellite location for an orbit at 45000 km altitude (*Didion et al.*, 2018). Each pixel in the airglow imager's FOV becomes an independent sensor providing timeseries of airglow perturbations which are proxies for atmospheric velocities or temperatures. Pixels can then be binned by a factor β to increase the SNR. Binning using $\beta \times \beta$ pixels increases the SNR by a factor β.

Finally, to account for the large FOV, we modify the surface area from airglow location $\mathbf{x}^{\text{airglow}}$ up to a distance r such that

$$\mathcal{S}^{\text{airglow}}(r, \mathbf{x}^{\text{airglow}}) \quad = \quad \mathcal{S}(r - r_0^{\text{airglow}}, \mathbf{x}^{\text{airglow}}) \cup \left[\mathcal{S}_{\text{FOV}}^{\text{airglow}}(\mathbf{x}^{\text{airglow}}) \cap \mathcal{S}_{\text{AEA}}^{\text{airglow}}(\mathbf{x}^{\text{airglow}})\right], \tag{D10}$$

where $\mathcal{S}_{\text{FOV}}^{\text{airglow}}(\mathbf{x}^{\text{airglow}})$ is a surface cap of radius $r_0^{\text{airglow}} \approx 70^\circ$ centered around the airglow imager location $\mathbf{x}$ and $\mathcal{S}_{\text{AEA}}^{\text{airglow}}(\mathbf{x}^{\text{airglow}})$ is the Airglow Emission Area (AEA) for each airglow layer. For the 1.27 μm emission, the AEA is centered on the equatorial point at 10:00 local time and covers an angular radius of about 60 degrees around that point and for the 4.28 μm emission, the AEA is centered on the equatorial point at 12:00 local time and covers an angular radius of about 70 degrees around that point (*Garcia et al.*, 2024).

Current mission concepts considering a stable high-altitude orbit at $R = 45\,000$ km (*Didion et al.*, 2018), which corresponds to an orbital velocity of about $v = \sqrt{GM/r} \approx 3.2$ km/s, where G is the gravitational constant, M the mass of Venus, and $r = R + R_v$ the distance from the center of Venus to the spacecraft where R_v is Venus' radius. This velocity translates into a ground velocity of about $2\pi r/v \approx 0.3$ km/s, i.e., 35 h to complete one orbit. The spacecraft will therefore probe both dayglow and airglow within a 2 day span.